D-148 Invited Paper

PHYSICS OF FLUIDS **26**, 101304 (2014)

Vorticity dynamics for transient high-pressure liquid injection[a)]

D. Jarrahbashi and W. A. Sirignano[b)]

Department of Mechanical and Aerospace Engineering, University of California, Irvine, California 92697, USA

(Received 19 April 2014; accepted 31 July 2014; published online 24 September 2014)

The liquid jet from a round orifice during the transient start-up and steady mass flux periods of a high pressure injector is studied via Navier-Stokes and level-set computations. Via post-processing, the role of vorticity dynamics is examined and shown to reveal crucial new insights. A brief review of relevant literature is made. An unsteady, axisymmetric full-jet case is solved. Then, a less computationally intensive case is studied with a segment of the jet core undergoing temporal instability; agreement with the full-jet calculation is satisfactory justifying the segment analysis for three-dimensional computation. The results for surface-shape development are in agreement with experimental observations and other three-dimensional computations; the initial, axisymmetric waves at the jet surface created by Kelvin-Helmholtz (KH) instability distort to cone shapes; next, three-dimensional character develops through an azimuthal instability that leads to the creation of streamwise vorticity, lobe shapes on the cones, and formation of liquid ligaments which extend from lobes on the cones. The cause of this azimuthal instability has been widely described as a Rayleigh-Taylor instability. However, additional and sometimes more important causes are identified here. Counter-rotating, streamwise vortices within and around the ligaments show a relationship in the instability behavior for jets flowing into like-density fluid; thus, density difference cannot explain fully the three-dimensional instability as previously suggested. Furthermore, the formation of ligaments that eventually break into droplets and the formation of streamwise vorticity are caused by the same vortical dynamics. Waviness is identified on the ligaments which should result in droplet formation. The nonlinear development of the shorter azimuthal waves and ligament waves explains the experimental results that droplet sizes are usually smaller than KH wavelengths. The higher the relative velocity and/or the lower the surface tension the shorter are the values of the most unstable wavelengths.
 [http://dx.doi.org/10.1063/1.4895781]

I. INTRODUCTION

Understanding, insights, and quantitative descriptions are needed to explain the factors that relate to the mechanisms for the hydrodynamic instability and eventual break-up of injected liquid streams at high pressure during both steady operation and transients (e.g., start-up and shut-down). The main goal of the present research is to investigate computationally a high velocity round jet injected into a quiescent high density gas for both steady and transient operation. In this work, special attention is given to the vorticity dynamics that explain the three-dimensional behavior and structures which develop following the initiating axisymmetric shear instability which we will identify as Kelvin-Helmholtz (KH) instability. Modifications of the vorticity field, and in particular,

[a)]This paper was presented as an invited talk at the 66th Annual Meeting of the APS Division of Fluid Dynamics, 24–26 November 2013, Pittsburgh, Pennsylvania, USA.

[b)]Electronic mail: sirignan@uci.edu.

the development of streamwise vorticity due to both baroclinic mechanisms (e.g., Rayleigh-Taylor instability) and strain-vorticity interaction, i.e., vortex tilting and stretching will be examined. The experimentally and computationally observed development[1–3] of cone-shapes, lobes, and ligaments on the liquid surface will be related to the vorticity dynamics.

The effects of bulk liquid jet acceleration during starting transient as well as local fluid accelerations will be considered. Here, Rayleigh-Taylor (RT) instability will not be related to gravitational acceleration. Rather, the fluid acceleration can be considered to produce a reversed D'alambert force. Attention will be given to the effects of surface tension and density difference between jet and ambient fluids. We are especially interested in high-density-gas applications, primarily because of the important application of injection and combustion of liquid fuels in high-pressure air. The Reynolds number and Weber number of interest will be sufficiently high that the Rayleigh capillary instability of the core jet would have too long a development time and would not occur before several other hydrodynamic instabilities appear; however, capillary instability on the thin ligaments can be of practical interest.

The present paper is organized as follows. Section II briefly comments on relevant literature. Computational methods are discussed in Sec. III. The results of the axisymmetric simulation of a single transient jet injected into high pressure quiescent air at very high *We* and *Re* during the start-up portion of the injection is described in Sec. IV. The penetration length of the transient jet and the range of observed wavelengths are compared with the experiments available in the literature. Moreover, different types of instability mechanisms are discussed in this section. In Sec. V, the valuable information obtained from the full transient jet simulations is used to develop a new model to capture the instabilities at the liquid/air interface with better resolution. In this new model, the instability is considered during the start-up period of injection for a segment of the axisymmetric jet whose fixed length is longer than the interesting wavelengths but still computationally manageable. This new model opens a new gateway for reducing the simulation costs, especially for three-dimensional simulations of the transient jet. The range of unstable wavelengths are compared favorably with the axisymmetric full jet simulations and linear instability theories.

The axisymmetric models for both full jet and liquid segment will be useful for predicting the initial Kelvin-Helmholtz (shear) instability and certain gross features of the flow. We shall see though that the three-dimensional liquid-segment calculations in Sec. VI will predict azimuthal waves and streamwise vorticity development appear on a shorter time scale than the secondary instabilities predicted by the axisymmetric computations. The three-dimensional computations will predict vorticity modification due to both Rayleigh-Taylor, (i.e., baroclinic) effects and strain-vorticity interactions. The results are compared to experimental observations. New information and insights are developed from post-processing of the data, especially with regard to determination of vorticity magnitude and direction and examination of vorticity production and modification by baroclinic effects and strain-vorticity interactions. Section VII gives a final overview.

II. LITERATURE REVIEW

Subsections II A–II D briefly review experimental research on liquid jets in gas environments, guidance from linear theory, computational research on the same subject for both round jets and certain specific planar configurations, and known behavior for jets flowing into like-density fluid.

A. Experimental studies on liquid jets

Different experimental techniques have been used in the literature to detect the differences between the jet structures during the transient period of injection compared to the steady-state.[4–11] The optical measurement techniques such as shadowgraph and Schlieren imaging and laser-based techniques, e.g., Mie scattering imaging and laser-induced fluorescence produce obscure images from the regions of high droplet density near the nozzle since the light scatters from the surface of the droplets. Therefore, these methods lack the sufficient detailed information about the spray structures near the nozzle. X-ray radiography techniques have been successfully applied to observe the instabilities of a diesel spray.[7,10,12,13] However, the two-dimensional images of high-pressure

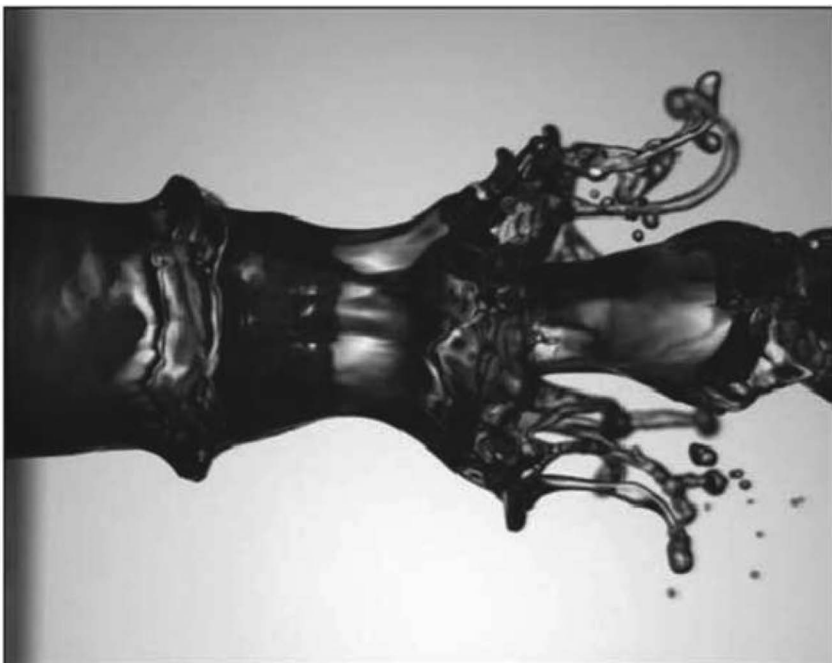

FIG. 1. Experimental results from coaxial flow of liquid and air. Lobe, ligament, and droplet formations. Reprinted with permission from P. Marmottant and E. Villermaux, "On spray formation," J. Fluid Mech. **498**, 73 (2004). Copyright 2004 Cambridge University Press.[1]

fuel sprays published so far do not reveal the small-scale structures of the near nozzle and high droplet density regions of the spray.

The ballistic imaging technique provides better images from the near nozzle structures compared to other optical techniques. The behavior of a single transient diesel spray during the injection process and the range of periodic wavelengths at the jet interface during start-up, steady-state, and the shut-down portions of the injection was observed by Linne *et al.*[14] via ballistic imaging techniques. They observed shorter wavelengths at the interfacial surface during the start-up compared with the steady-state period of injection.

Marmottant and Villermaux[1] exposed liquid jets with various diameters to a fast parallel gas flow. Informative images were obtained in Reynolds and Weber number ranges where droplet density remained low. In their co-flow experiment, the velocity of the liquid and air were 0.6 m/s and 35 m/s, respectively. The gas-to-liquid density ratio, gas-to-liquid viscosity ratio, *Re* and *We* were 0.00125, 0.016, 410, and 40, respectively. The diameter of the liquid jet in their experiment used as the reference length was 7.8 mm. They found that the atomization process consisted of several stages as indicated in Fig. 1: first, a shear (KH) instability led to formation of primary waves at the interface which distorted to form cones; second, the conical crests of these waves developed an azimuthal instability which the authors suggested was a RT instability. They observed that this secondary instability occurs after the primary KH wave crests become cone-shaped. The measured azimuthal wavelengths were in a magnitude regime consistent with that mechanism. This secondary instability resulted in a three-dimensional departure from axisymmetry with the formation of lobes on the conical crests whose cross dimensions were determined by the azimuthal wavelength. They observed that, unlike the shear instability at the interface, the secondary wavelengths depended strongly on the surface tension. Further extension of the lobes resulted in the formation of long, thin ligaments protruding from the lobes on the conical crest. These extended ligaments eventually break into droplets. The mean droplet size distribution proposed by Marmottant and Villermaux[1] is given by the length of the supposed RT instability wavelengths. Therefore, the study of the secondary instability in a jet can improve the prediction of the size of the liquid ligaments that extend from the jet core and eventually break-up to form the droplets.

Experimental researchers[1,15] have estimated fluid acceleration normal to the liquid-gas interface to predict Rayleigh-Taylor wavelengths which can be compared to the observed shorter wavelengths on the jet lobes. As we note later, it is actually the tangential acceleration which is relevant to the stability; however, in our calculations, normal and tangential fluid accelerations at the crest of the KH surface waves were commonly of the same order of magnitude. No previous attempt has been made to compare baroclinic-vorticity generation with vorticity generated by strain-vorticity interaction. Note also that it would be difficult to measure tangential velocity, vorticity, or strain on and near the liquid-gas interface in an experiment.

B. Guidance from linear theory

Although the research to be discussed will address nonlinear behavior and couplings between different instability mechanisms, it is useful to examine the predictions of linear theory especially in terms of wavelengths with fastest growth rates.

There are four physical phenomena which contribute to the hydrodynamic instabilities: (1) inertial difference across the shear layer at the jet interface, i.e., Kelvin-Helmholtz (shear) instability; (2) acceleration tangent to the interface, i.e., RT instability; (3) capillary effects; and (4) viscous effects. The four related terms appear proportional to wave number to the second, first, third, and fourth power, respectively in Eq. (1). That equation is the dispersion relation obtained for viscous potential flow (and not therefore for shear flow) by Joseph *et al.*[16] So, viscous effects dominate at very short wavelengths while acceleration effects dominate at very long wavelengths and surface tension has stabilizing effects on shorter wavelengths. While Eq. (1) strictly applies to an initially planar interface, it provides a useful guide for evaluation of the physics. The following dispersion relation depicts the relation between temporal growth rate and wave number;

$$\omega = -k^2\frac{\mu_l+\mu_g}{\rho_l+\rho_g} \pm \left[\rho_l\rho_g k^2\left(\frac{u_g-u_l}{\rho_l+\rho_g}\right)^2 - k\frac{\rho_l-\rho_g}{\rho_l+\rho_g}g - \frac{k^3\sigma}{\rho_l+\rho_g} + k^4\left(\frac{\mu_l+\mu_g}{\rho_l+\rho_g}\right)^2\right]^{1/2}, \tag{1}$$

where ω is the temporal growth rate, μ and ρ are the viscosity and density, and the indices l and g refer to liquid and gas, respectively. σ is the surface tension coefficient, and k is the wave number. g is the gravitational acceleration that can be replaced by the acceleration of the light fluid directed into the heavy liquid since this acceleration is considerably greater than gravitational acceleration as our simulation demonstrates. If an acceleration much larger than gravitational acceleration is applied, short wavelengths can be experienced; this is the situation in the transient jet considered here. The acceleration term is destabilizing (stabilizing) when the heavier (lighter) fluid accelerates into the lighter (heavier) fluid.[17,18]

The RT instability can result from the fluid accelerations at the liquid interface that has been exposed to the primary Kelvin-Helmholtz (shear) instability. That instability can be viewed as a baroclinic effect due to the cross product of the density gradient (which is normal to the surface) and a component of the pressure gradient tangent to the surface. The pressure gradient can be represented in terms of a body force or a fluid acceleration. Although the literature commonly discusses the normal component of the body force or fluid acceleration at the surface, a perturbation of the local surface orientation causing a misalignment of density gradient and pressure gradient is required to drive the instability.

The classical KH instability is a shear instability in the limit of zero shear-layer thickness of the interface of two fluids with a velocity discontinuity. In reality, two adjacent boundary layers with different thicknesses form at the interface and both velocity and the shear stress are continuous. The effects of this finite-size shear layer on the instability of two parallel streams with same densities was first investigated by Rayleigh.[19] Marmottant and Villermaux[1] have analysed the transition between the classical KH and Rayleigh instability for two parallel streams and proposed a criterion based on the liquid density ratios, vorticity or shear-layer thickness and the velocity of the less dense fluid, and the surface tension. The Rayleigh instability overcomes the classical KH instability as long as $(\sigma/\rho_g u_g^2 < \delta(\rho_l/\rho_g)^{1/2})$, where ρ_l and ρ_g are the density of liquid and gas, respectively, σ is the

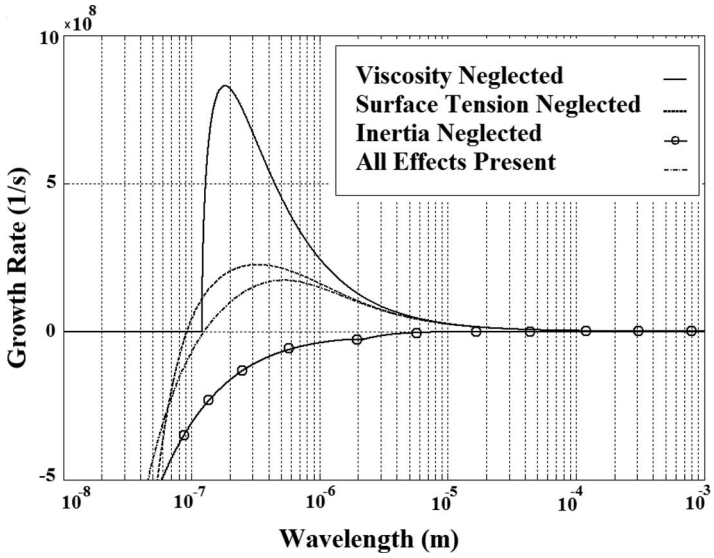

FIG. 2. Real part of the linear growth rate as a function of wavelength based on VPF instability analysis.[16]

surface tension coefficient, δ is the gas shear layer thickness, and u_g is the gas velocity. The above mentioned criterion is satisfied in our case; so, the shear instability lies within the Rayleigh limit.

Fig. 2 shows a plot of the real part of the growth rate versus wavelength based on Joseph, Belanger, and Beavers[16] using the parameters mentioned in Table I, *Re* and *We* equal 16 000 and 230 000, respectively. (See Sec. III for definition of non-dimensional groups.) Acceleration is taken equal to 800 000 m/s^2, approximate value of the liquid jet acceleration through the orifice of a typical diesel engine injector averaged during start-up, i.e., 300 μs. u_l and u_g equal to 200 m/s and zero, respectively. Positive values of growth rate indicate the instability region. Clearly, at sub-micrometer wavelengths, where viscosity and capillary effects dominate, it shows stable behavior. The dispersion relation reflected in Eq. (1) accounts for both KH and RT instabilities. This figure clearly shows that instabilities are expected in the wavelength range that are commonly found in simulations, i.e., O(10^{-6}–10^{-4} m).

For sub-millimeter, super-micrometer wavelength range of interest, unlike the liquid acceleration, viscosity and surface tension are very important. Based on the results obtained from our present work, the effects of acceleration are more significant at early times of injection. At the beginning of injection period when the jet velocity is small, e.g., 0–30 m/s, compared to the maximum jet velocity at the end of start-up period, i.e., 200 m/s at 300 μs, the acceleration is of the order 10^5–10^6 m/s^2. With a reference length comparable to the orifice diameter (e.g., 200 μm), in non-dimensional form the inertia effects are less significant. Certainly, for higher jet velocity, i.e., later injection times, the inertia effects will overcome the acceleration effects. In other words, neglecting the jet acceleration term in the dispersion equation has no significant effect on the linear growth rate for later times of transient injection. This is consistent with the previous studies that showed acceleration did not have a noticeable effect on the break-up length or the overall characteristics of the transient liquid jet.[20] However, the liquid acceleration caused by the instability can be responsible for producing small-scale instabilities at the interface.

TABLE I. Fluid properties.

Fluid properties	Liquid	Air
Viscosity (kg/m s)	1.64×10^{-3}	1.85×10^{-5}
Density (kg/m^3)	804	38.4 at 30 atm
Surface tension coefficient (N/m)	0.028	...
Maximum jet velocity (m/s)	200	...

The capillary instability of a cylindrical jet depends on the liquid viscosity. The capillary break-up time of a liquid jet can be defined as follows as indicated by Marmottant and Villermaux:[1] $t_\sigma = \sqrt{\frac{\rho_l D^3}{\sigma}} f(Re)$, where D, ρ_l, and σ, represent the jet diameter, liquid density, and surface tension coefficient, respectively, and Re is defined as $Re = \sqrt{\frac{D\sigma\rho_l}{2\mu_l^2}}$. The linear instability analysis by Chandrasekhar[21] predicts the maximum growth rate and most unstable wavelengths.[1] Based on the values reported in Table I, the most unstable wavelength and capillary break-up time for a 200 μm diameter segment equals to 467 μm and 0.55 ms, respectively. Therefore, for the range of observed wavelengths during the start-up period of injection, the capillary break-up time is larger than the start-up period in our simulations, i.e., 0.3 ms. Therefore, capillary instability is not responsible for the jet core instability, especially during the start-up period. However, the capillary effect can be important for the ligament break-up.[1]

C. Computational studies on liquid jets and streams

Most of the numerical studies on transient jet behavior are based on the extension of the steady-state break-up model that, in turn, is dependent on empirical constants obtained from the experiments. Abani and Reitz[22] formulated a new break-up model for unsteady axisymmetric turbulent jets based on an extension of steady-state. Turner *et al.*[20] studied the effects of acceleration on the break-up lengths and time for planar liquid jets by implementing a wave-packet analysis on the disturbances initiated from the orifice. They showed that the unsteady effects of the jet is noticeable for high accelerations and high liquid-to-air density ratios, especially at early stages of the injection. They also reported that for later times of injection when the velocity profile varies slowly with time, the overall characteristics of the unsteady jet, e.g., the break-up lengths and time were not affected significantly compared to the quasi-steady jet. Turner *et al.*[23] predicted the transient jet break-up length and its penetration into the gas by proposing a composite break-up model that showed more consistency with the experiments. They defined the break-up time and length of the jet based on a linear instability analysis considering the effects of the gas shear layer in their basic velocity profile. They also showed that the transient behavior of the jet plays an insignificant role in the overall break-up length of the jet. However, the crucial effects of the acceleration in the initial stripping of the droplets from the coherent jet before it breaks up should be studied thoroughly.

A balanced-force Refined Level Set Grid (RLSG) method developed by Herrmann[24] is shown to be an accurate tool to capture the complexities at the interface for two-phase flow simulations. The three-dimensional simulation of primary atomization of turbulent liquid jets using the same method by Herrmann[3] is a promising tool to describe the primary instabilities of a turbulent liquid jet injected into quiescent air. During atomization, the phase interface exhibits a highly complex, three-dimensional surface with a large range of different scales. Drop-size distribution was reported by investigating the secondary atomization of the droplets and small particles by transferring them into a Lagrangian frame. Herrmann[3] concluded that the current prediction of very small-scale wavelengths is mesh-size dependent even by using RLSG method. It is widely agreed that one of the challenges of the numerical simulation of jet atomization is the artificial break-up of the ligaments where cross dimensions become comparable to mesh size. This concern has been reported by Shinjo and Umemura,[2] Herrmann,[3,24] and Gorokhovski and Herrmann.[25] As discussed in these papers, by refining the grid spacing, the results improve; however, the artificial and non-physical break-up of the small-scale ligaments and droplets comparable to the grid size is still a concern. Thus, the predicted break-up of these ligaments is dependent on the grid resolution. A coarse grid produces thicker ligaments and larger droplets when detached from the jet core since the artificial break-up occurs when the thickness of the liquid becomes comparable to the grid size. However, according to Shinjo and Umemura[2] for three-dimensional computations, if the size of the ligaments and droplets is in a range where only surface tension dominates the break-up, i.e., small waves can be detected on the ligaments and the detached liquid droplets are spherical, the numerical simulation is physically accurate and grid-spacing is sufficient. However, the proper criterion for concluding that the ligament break-up is sufficiently resolved is the accurate capture of the growth of a capillary

instability on the ligament surface. A finer mesh would be needed to predict droplet formation from the ligaments although the growth of instability on ligaments has already been captured with the present calculation. It should be noted that, while the phenomenon of ligament break-up is always mesh-dependent, if one captures the onset of the Rayleigh-Plateau instability, then the rapid growth of the instability will ensure that the resulting drops do not depend strongly on the mesh size.

Studies of Shinjo and Umemura[2] on three-dimensional simulation of the primary atomization of a liquid jet injected into quiescent air is one of the most advanced simulations in this field. Their fine grid resolution captures the description of ligament formation and droplet detachment from the jet core; yet, it is very demanding in terms of the computer resources. The effects of the jet core acceleration on the liquid atomization has not been investigated by Shinjo and Umemura[2] and Herrmann.[3] The temporal instability of a planar turbulent liquid jet investigated by Pitsch and Desjardins[26] is helpful to understand the primary instability of round jets. They addressed a low range of Weber number values, i.e., $We \leq 2000$. They found that punctures resulted in the surface of the ligaments and inflated to form thin-membrane structures filled with gas on one side of the ligament. These structures sometimes separated forming bubbles and later burst. Other experimental[1] and computational research[2,3] at higher Weber number values did not show these structures.

Some effects of viscosity can be remarkably well represented by viscous potential flow (VPF) instability analysis.[27,28] Joseph, Belanger, and Beavers[16] investigated the secondary break-up of both Newtonian and non-Newtonian droplets in a shock tube exposed to very high accelerations of orders 10^4 to 10^5 times the gravity. They claimed that the RT instability is the main cause of the break-up. Varga, Lasheras, and Hopfinger[15] described the break-up of a small-diameter liquid jet exposed to high-speed gas jet as secondary RT instability of the primary KH instability. They proposed a break-up model for the initial droplet size assuming inviscid liquid based on the same acceleration mechanism that breaks up liquid droplets in high speed airstream investigated by Joseph, Huang, and Candler[29] and Joseph, Belanger, and Beavers.[16] The Varga, Lasheras, and Hopfinger model[15] was based on the classic linear stability analysis by Chandrasekhar,[21] including the effects of surface tension. The RT instability dispersion relation and wavelength has been predicted as follows:

$$\omega = \left[\frac{k(\rho_l - \rho_g)a_n - k^3\sigma}{\rho_l + \rho_g}\right]^{1/2}, \tag{2a}$$

$$\lambda_{RT} = 2\pi\sqrt{\frac{3\sigma}{(\rho_l - \rho_g)a_n}}, \tag{2b}$$

where λ_{RT} is the most unstable RT wavelengths and a_n is the acceleration perpendicular to the liquid interface. This formulation neglects the effects of viscosity on jet instability unlike the VPF dispersion relation, Eq. (1), it predicts the range of RT wavelengths directly from measuring the normal acceleration of the ligaments. Equation (2b) has been extensively used in the literature as a means to estimate the theoretical RT wavelengths compared to numerical or experimental observations.[1,15,23,30–32] The omission of the tangential component of acceleration at the interface raised a theoretical concern described in Subsection II B. Varga, Lasheras, and Hopfinger[15] observed that the RT instability wavelengths generated on the wave crests resulted from the primary KH instability is proportional to the primary mean droplet sizes. According to Varga, Lasheras, and Hopfinger[15] the scale of the primary mean droplet sizes, i.e., Sauter Mean Diameter (SMD), during the primary atomization process are close to the most unstable RT wavelength; they suggested $SMD \approx \lambda_{RT}/5$, consistent with their experiment.

Fig. 3 shows results for a two-dimensional vorticity dynamics calculation by Rangel and Sirignano.[33] Gas flows above the interface to the right while liquid flows below to the left. The interface development is on the left in the figure and shows that, as surface tension increases (i.e., their parameter W increases), the surface curling is inhibited. Still, a cone shape forms which is similar in cross-section to what is observed in the early axisymmetric behavior of the round liquid jet. The sub-figures on the right show that vorticity becomes less concentrated with increasing surface tension. Still, concentrations of vorticity are seen in two places for the highest value of surface

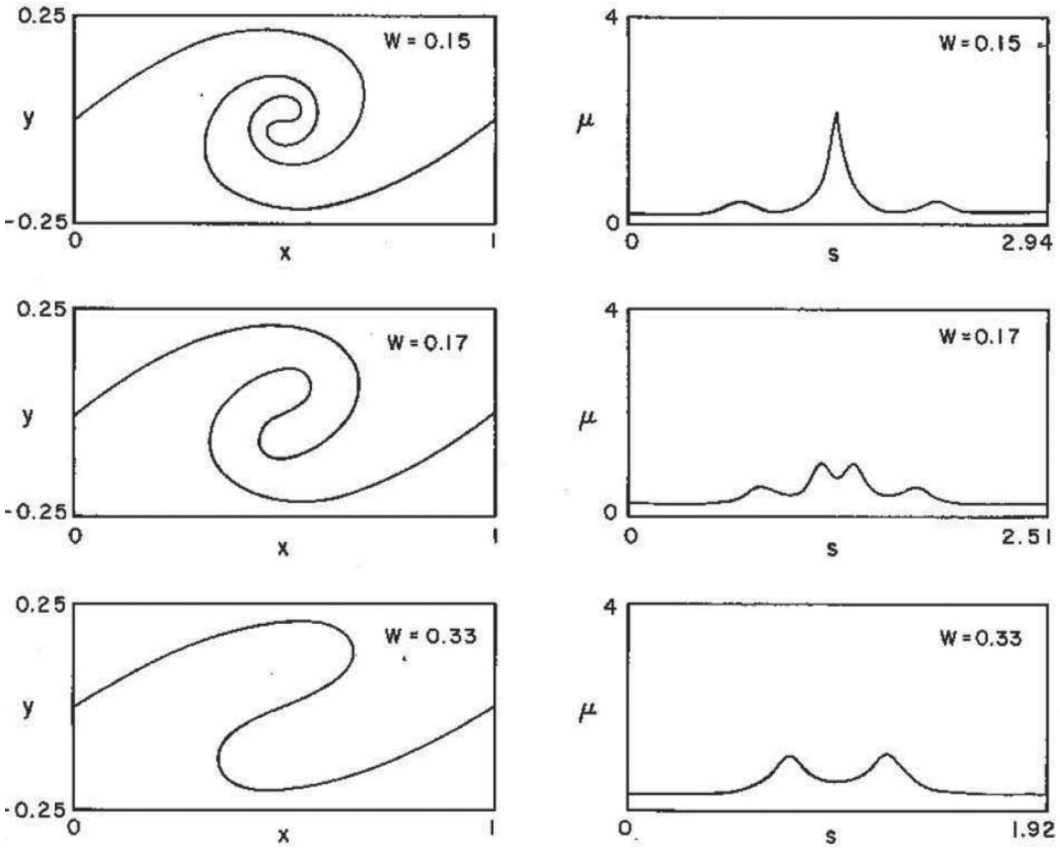

FIG. 3. Two-dimensional nonlinear KH behavior with surface tension and density difference. Interface development (left) and vorticity distribution (right). Reprinted with permission from R. H. Rangel and W. A. Sirignano, "Nonlinear growth of Kelvin-Helmholtz instability: Effect of surface tension and density ratio," Phys. Fluids **94**, 1845 (1988). Copyright 1988 AIP Publishing LLC.[33]

tension, in the braid and at the crest. Rangel and Sirignano[34] extended this analysis to liquid sheets and found similar behavior on two interfaces.

Rangel and Sirignano[33,34] treated the liquid-gas interfaces as vortex sheets and calculated the local circulation per unit length of the vortex sheet using a formula developed by Rottman and Olfe[35] and Zalosh:[36]

$$\frac{\Delta\Gamma}{\Delta t} = 2\frac{\rho_g - \rho_l}{\rho_g + \rho_l}\left(\frac{du}{dt}\right)_s \Delta s + \frac{1}{4}\frac{\rho_g - \rho_l}{\rho_g + \rho_l}\frac{\partial}{\partial s}\left(\frac{\Delta\Gamma}{\Delta s}\right)^2 \Delta s - \frac{2}{We}\frac{\partial\kappa}{\partial s}\Delta s, \tag{3}$$

where Γ, ρ_g, ρ_l, s, We, and κ are, respectively, the circulation of an infinitesimal section of the vortex sheet (also known as liquid-gas interfacial surface), gas density, liquid density, arc length along the surface, Weber number, and local surface curvature. $(du/dt)_s$ is the acceleration of the fluid at the sheet in a parallel direction to the sheet. Due to the velocity discontinuity in the inviscid theory, this acceleration is the average of the two accelerations from the two sides of the sheet. It is positive when directed in the positive s-direction. Equation (3) shows that in two dimensions, the first two terms on the right side depend on density difference across the vortex sheet while the last term depends on surface tension. The first two terms are baroclinic effects. A pressure gradient component parallel to the sheet surface can relate to the fluid acceleration through the first term or to a spatially varying circulation through the second term. Both spatial and temporal velocity-derivative terms balance with the pressure gradient in the momentum equation. In two dimensions, the interaction between strain and vorticity does not affect vorticity development; so, no term of that vortex-stretching type appears in the equation.

If there is a body force, the local tangential component of the acceleration at the sheet due to the body force should be subtracted from the fluid acceleration in the first term on the right side of Eq. (3). Realize that the tangential component and not the normal component of the body force is relevant here. Classical linear theory uses the normal component body force for an initially horizontal surface; it predicts the stability of a small perturbation. However, any perturbation, no matter how small, should create a slant or waviness to the surface. Then, a tangential component appears in some localities and determines the stability. Tryggvason[37] considered a two-dimensional fluid subjected to Rayleigh-Taylor instability. He used a vortex dynamics method similar to Rangel and Sirignano, properly using the tangential component of the body force at the surface to drive the instability.

D. Jets flowing into fluids with like density

Liepmann and Gharib[38] studied a water jet flowing into a water tank using LIF imagining. Figs. 4 and 5 come from their work. The initial vortex rings remain axisymmetric for a short distance until an azimuthal instability occurs. The secondary instability first develops in the braid region between vortex rings producing streamwise vorticity. Azimuthal instabilities also develop from the rings although more slowly than in the braid region. This behavior is similar to the vortical structures observed in three-dimensional mixing layers.[39] Bernal and Roshko[39] noticed that the streamwise vortex is actually a hairpin vortex that wraps around the primary spanwise vortices. The hairpin vortex changes direction and thereby produces counter-rotating vortex pairs in the streamwise direction. A schematic of hairpin vortices from Bernal and Roshko[39] is shown in Fig. 6. Liepmann and Gharib[38] did not discuss hairpin vortices for the round jet in connection with streamwise counter-rotating vortex pairing. However, we will later in Sec. VI investigate their existence and importance for the round jet. Cai, Tsai, and Liu[40] numerically investigated the vorticity dynamics of a jet injected through a circular, V-shaped, and A-shaped notched nozzles into a same density environment. Their results for the circular nozzle agreed with the experiments of Liepmann and Gharib. They observed the same distribution of the counter-rotating streamwise vortex pairs in the azimuthal direction.

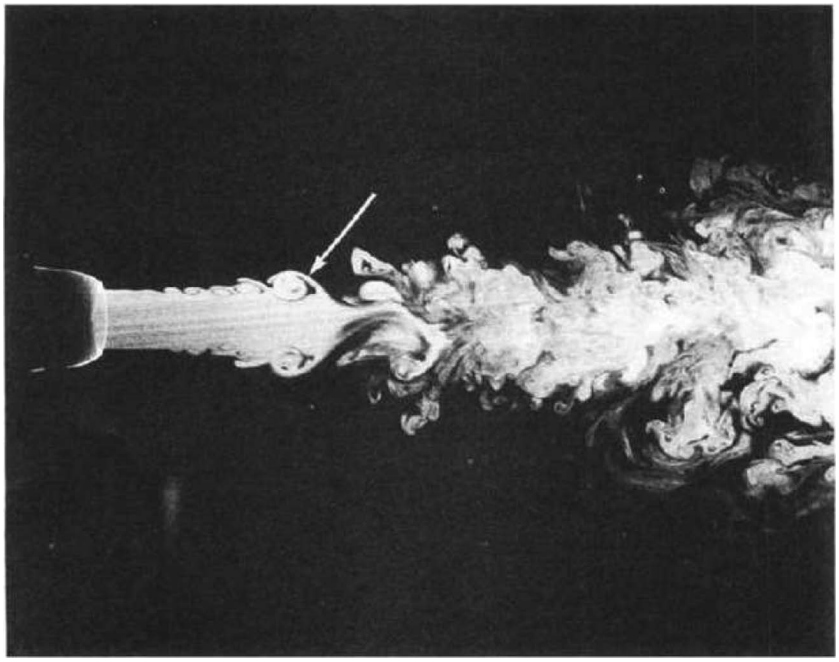

FIG. 4. Three-dimensional jet behavior for water flowing into water. Reprinted with permission from D. Liepmann and M. Gharib, "The role of streamwise vorticity in the near-field entrainment of round jets," J. Fluid Mech. **245**, 643 (1992). Copyright 1992 Cambridge University Press.[38]

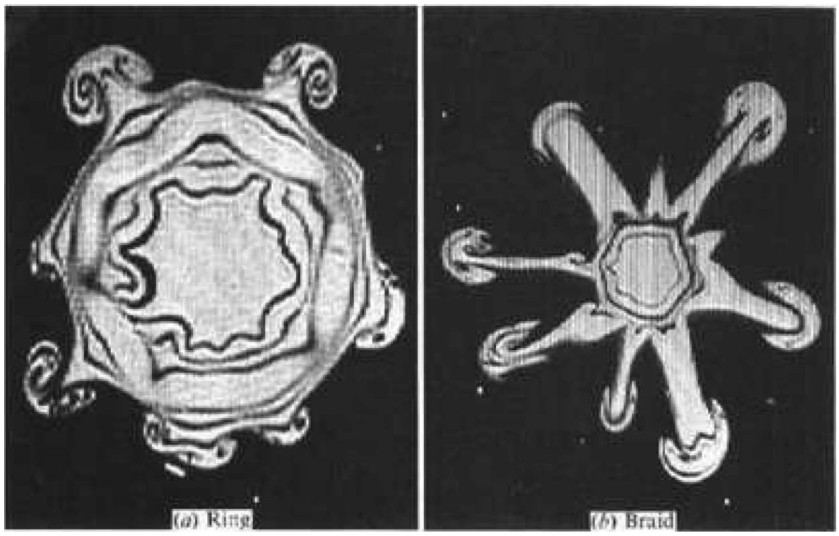

FIG. 5. Cross-section for three-dimensional jet behavior for water flowing into water. Counter-rotating vortices in ring (left) and braid (right). Reprinted with permission from D. Liepmann and M. Gharib, "The role of streamwise vorticity in the near-field entrainment of round jets," J. Fluid Mech. **245**, 643 (1992). Copyright 1992 Cambridge University Press.[38]

The interaction of the streamwise vortex with the primary vortex rings leads to the distortion and stretch of the primary vortex rings at an angle with respect to the jet axis. Counter-rotating vortex pairs occur in each structure shown in Fig. 5; these new structures are sometimes called side jets.[41–45] Side jets have also been observed experimentally[46] for non-homogenous jets with a very small density difference, i.e., cold and hot jets. Later, we shall examine the liquid jet into a gas and find indications that these side jets from the rings result in the ligament formation.

The onset of the azimuthal instability of the three-dimensional jet is known as the deformation of the primary axisymmetric vortex rings first observed experimentally by Widnall, Bliss, and Tsai.[47] They noticed that the vortex ring is unstable to bending waves. They proposed a simple theoretical model that predicted the unstable modes that were observed in experiments. The wave number of the most amplified mode was dependent on the radius of the vortex ring. In another attempt to formulate the growth rate of the three-dimensional instability of vortex rings, they investigated the

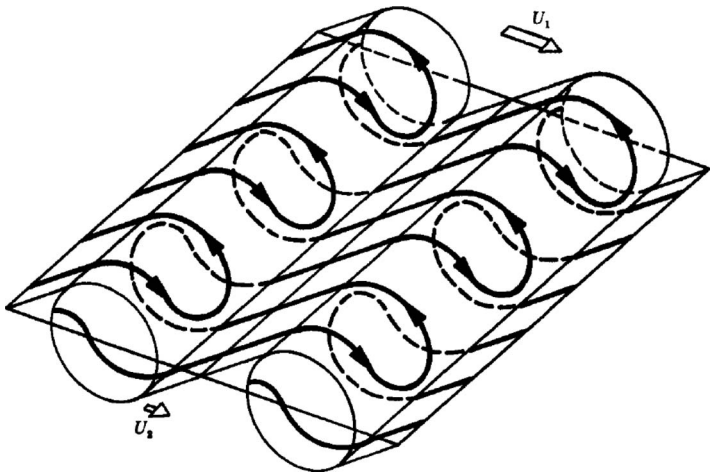

FIG. 6. Topology of streamwise vortex lines showing hairpin vortices in three-dimensional mixing layers. Reprinted with permission from L. P. Bernal and A. Roshko, "Streamwise vortex structure in plane mixing layers," J. Fluid Mech. **170**, 499 (1986). Copyright 1986 Cambridge University Press.[39]

instability of a straight vortex tube subjected to a perturbed strain field.[48] For a small-diameter vortex tube, the analysis was assumed to be consistent with the vortex ring instability. They predicted the amplification rate of the short-wave instability on the vortex tube based on a linear instability analysis and showed that the amplification rate is proportional to the rate of strain.

The azimuthal mode number is equivalent to the number of lobes of the deformed vortex ring. The mode number predicted by Widnall varied between 7 and 9. The experimental observation by Dazin, Dupont, and Stansilas[49] on the instability of the water vortex rings into water indicated a band of unstable modes between 7 and 10. Their results also showed that the amplification factor proposed by linear inviscid instability theories is higher than their experiments since viscosity attenuates the growth rate. Therefore, while viscosity does not play a significant role at the onset of the azimuthal instability, it later decreases the growth rate of the instability.

Numerical simulation of homogenous jets showed different modes of the azimuthal instability.[43–45] Abid and Brachet[43] showed that initial perturbations with azimuthal wave number equal to three, four, and six produced three, four, and six liquid side jets, respectively. Numerical investigations of the three-dimensional homogenous round jets exposed to azimuthal and streamwise perturbation by Brancher, Chomaz, and Huerre[44] showed that the most unstable mode was three. Unforced simulations of Danaila, Dusek, and Anselmet[45] predicted a mode number equal to four for homogenous jet. The number of streamwise vortex pairs were consistent with the mode number in numerical simulations.[43–45] Therefore, although Widnall instability plays an important role in producing the azimuthal instability on the vortex ring, formation of streamwise counter-rotating vortex pairs is responsible for generation of the side jets.[38,41,44] Experimental observations[38] and numerical computations[45] have shown that the number of the lobes increases by increasing the jet Reynolds number. Danaila, Dusek, and Anselmet[45] tested the effects of the orientation and number of the computational elements in their simulations and proved that azimuthal mode number equal to four was one of the possible unstable modes, i.e., "natural mode" for non-perturbed homogenous jet flow.

There is indication here from homogenous round jets that strong azimuthal instabilities can synergize with the earlier KH instability even if no density difference occurs. Thus, we cannot conclude without more evidence that the azimuthal instabilities on liquid jets flowing into a gas are primarily the result of a Rayleigh-Taylor instability. There are two mechanisms which can create azimuthal vortical structures: baroclinic effects and strain-vorticity interactions. With like density, only the latter appears. Baroclinic effects can be expected when density differences are present but there is no reason to conclude that the latter mechanism disappears when density differences occur. Previous researchers on liquid jet flows have not attempted to separate the potential causes of three-dimensional instability. That path is now pursued here.

We shall relate the formation of lobes and ligaments to the development of side jets with counter-rotating streamwise vortex pairs. Thereby, a relationship between two-phase jet flows and single-phase jet flows will be identified and explained. Surface tension will be shown to have important effects.

III. COMPUTATIONAL METHOD AND CONFIGURATION

The Navier-Stokes and continuity equations for an incompressible flow follows:

$$\rho\frac{\partial \mathbf{u}}{\partial t} + \rho(\mathbf{u}\cdot\nabla)\mathbf{u} = -\nabla p + \mu\nabla^2\mathbf{u} + \mathbf{F}; \quad \nabla\cdot\mathbf{u} = 0, \tag{4a}$$

$$\rho\frac{D\mathbf{u}}{Dt} = -\nabla p + \mu\nabla^2\mathbf{u} - \sigma\kappa\delta(d)\mathbf{n}, \tag{4b}$$

where $\mathbf{u}$ is the velocity field; ρ and μ are the density and dynamic viscosity of the fluid, respectively. p is the pressure and $\mathbf{F}$ is the body force applied to the fluid. In addition, the surface-tension force applied on the interface is defined based on the level-set function and curvature of the interface as is shown in the third term on the right-hand side of the Navier-Stokes equation (4b), where σ is the surface tension coefficient, δ is the delta function, d represents the distance from the interface, $\mathbf{n}$ and

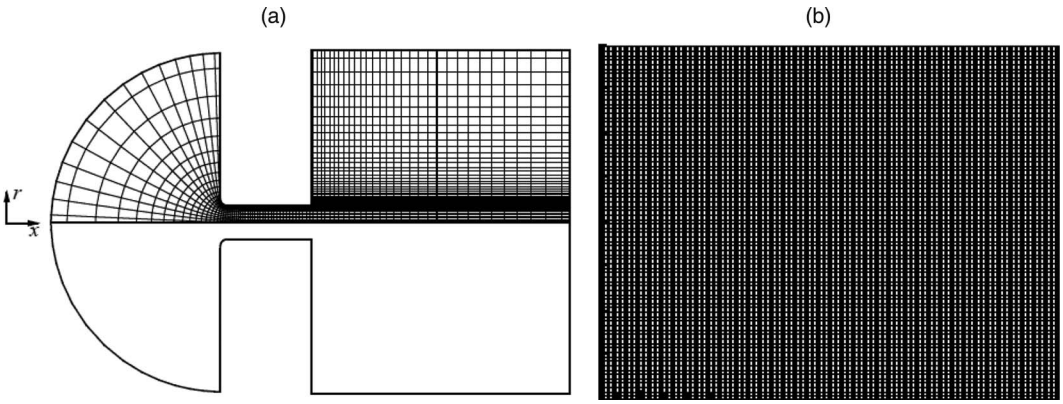

FIG. 7. Physical domain and orthogonal grid (a) orifice and gas chamber for full jet (flow from left to right) (b) liquid-segment model.

κ are the normal vector directing toward the gas phase and the curvature of the interface, respectively. A finite-volume discretization on a staggered grid has been considered. The convection-diffusion problem has been discretized based on the finite-volume method using the QUICK algorithm[50] and the Crank-Nicolson scheme for discretizing the unsteady term. The coupling of the continuity and momentum equations is done through the SIMPLE algorithm.[51] The level-set method developed by Sussman *et al.*[52] and Osher and Fedkiw[53] tracks the liquid/gas interface. The level-set is a distance function with zero value at the liquid/gas interface; positive values in the gas phase and negative values in the liquid phase. It is denoted by θ and all the fluid properties for both phases in the Navier-Stokes equations can be defined based on its values and the equations could be solved for both phases simultaneously. Properties such as density and viscosity will be allowed to vary continuously but with a very large gradient through a thin region at the liquid-gas interface. The level-set function is also convected by the unknown velocity field based on the following equation:

$$\frac{\partial \theta}{\partial t} + \mathbf{u} \cdot \nabla \theta = 0. \tag{5}$$

For detailed descriptions on interface tracking, see Refs. 54–56.

The computational domain and gridding system that consists of an orifice initially full of liquid and a gas chamber initially filled with quiescent gas is demonstrated in Fig. 7(a). The plenum pressure upstream in the orifice is set to increase exponentially over a period of 0.3 ms until a prescribed maximum pressure is reached after which the plenum pressure is held constant at that cap value for another 0.1 ms. The plenum pressure drives the flow and the mass flux; the exit velocity of the jet increases with the plenum pressure. At the end of the start-up process, the maximum jet velocity reaches 200 m/s. The no-slip boundary condition on the orifice channel wall and slip condition on the outer boundary of the gas chamber have been applied. The velocity and viscous stress are continuous at the liquid/gas interface. The computational grid consists of an orthogonal coordinate system based on potential-flow solutions in the orifice[54] and an orthogonal cylindrical axisymmetric system in the external flow. There are 4000 and 600 mesh points in the x- and r-direction, with 9600 mesh points lying in the orifice and orifice channel and 2 390 400 in the external flow. The flow properties are summarized in Table I.

Re, *We*, and *Fr* have been defined as follows: $Re = \frac{\rho_l \overline{u} D}{\mu_l}$, $We = \frac{\rho_l \overline{u}^2 D}{\sigma}$, $Fr = \sqrt{\frac{\overline{u}\tau}{D}} = \frac{\overline{u}}{\sqrt{aD}}$, where $\overline{u}$, ρ_l, μ_l, σ, D, a, and τ are the mean exit plane velocity corresponding to the maximum mass flow rate, the liquid density, liquid viscosity, surface tension coefficient, orifice diameter, mean local exit fluid acceleration, and time required for the liquid jet velocity transition from zero to $\overline{u}$ at the orifice exit, respectively.

Predicting the jet instability during steady-state followed by the shut-down process requires the length of the gas chamber to be more than 200 times the orifice diameter which would increase the cost of the simulations significantly. Therefore, the information obtained from the full transient jet

simulations described above has been used to develop a new model to capture the instabilities at the liquid/gas interface with better resolution and lower cost than for the full jet computations. In this new model, a segment of the jet whose fixed length is longer than the interesting wavelengths but still computationally manageable, e.g., 1-mm length for a 200-μm initial diameter will be considered during the start-up period of jet injection as shown in Fig. 7(b).

To consider the effects of acceleration on the fluid motion of this segment, the frame of reference has been transferred from the laboratory frame identified with $(\mathbf{x}, t)$ and the fluid velocity $\mathbf{U}(\mathbf{x}, t)$ to an accelerating frame in which the mass center of the segment is stationary, identified with $(\mathbf{X}, t)$ and $\mathbf{v}(\mathbf{X}, t)$ where $\mathbf{v}(\mathbf{X}, t) = \mathbf{U}(\mathbf{x}, t) + \mathbf{V}(t)$ and $d\mathbf{X} = d\mathbf{x} + \mathbf{V}(t)dt$. $\mathbf{V}(t)$ is the liquid injection velocity at the orifice exit that varies with time only. In other words, all the liquid particles are assumed to travel with the same velocity as the liquid jet exit. Substituting $\mathbf{v}(\mathbf{X}, t) = \mathbf{U}(\mathbf{x}, t) + \mathbf{V}(t)$ in Eq. (4a) and considering the fact that the spatial derivative of $\mathbf{V}(t)$ is zero, the resultant modified Navier-Stokes and continuity equations are shown in Eq. (6). This transformation generates a new term $\rho\dot{\mathbf{V}}$ as a generalized body force in the equations of motion. $\dot{\mathbf{V}}$ is the acceleration of the frame of reference equivalent to the acceleration of the liquid jet emerging from the orifice that will be determined based on the full transient jet simulations. ρ is the density of the liquid/gas that will be determined based on the values of the level-set function discussed earlier,

$$\rho\frac{D\mathbf{U}}{Dt} = -\nabla p + \mu\nabla^2\mathbf{U} - \sigma\kappa\delta(d)\mathbf{n} - \rho\dot{\mathbf{V}}; \quad \nabla\cdot\mathbf{U} = 0. \tag{6}$$

The fluid segment consists initially of two concentric cylinders; liquid is in the inner cylinder and the gas fills the surrounding outer cylinder. In our first calculations, the diameters of the inner and outer cylinders are 200 and 800 μm, respectively, and the length of the liquid segment is 1 mm. The liquid-segment diameter is consistent with the jet-orifice diameter used in full jet simulation. The total number of mesh points is 400 000 (1000 in x-direction and 400 in r-direction); the computational grid consists of a uniform mesh ($\Delta x = \Delta r = 1$ μm).

The same scheme used for full jet simulations will be used for liquid-segment; now, the effects of constant body force given in Eq. (6) have been considered. The liquid is initially stationary and the gas flows over the interface from right to left in Fig. 7(b) with a starting value associated with the velocity of the liquid jet on the axis of symmetry and acceleration of the liquid jet obtained from the full jet analysis when the jet has penetrated about 1 mm into the gas. The periodic conditions for pressure gradient and velocity at the right and left boundaries and the symmetry boundary condition at the bottom boundary (axis of jet) of the computational domain have been applied. In addition, the normal gradient of velocity is zero on the outer boundary. Unlike the velocity, pressure is not periodic; a pressure change is needed to balance the acceleration term. The results from this axisymmetric liquid-segment model will be discussed in Sec. V.

IV. FULL TRANSIENT JET

The axisymmetric CFD code mentioned in Sec. III has been developed to simulate the flow of a liquid through an orifice and the gas chamber during start-up, steady-state, and shut-down period of injection. The fluid properties and the computational domain are shown in Table I and Fig. 7(a), respectively. Grid spacing is 1 μm in the major flow direction and varies from 1 to 2 μm in the radial transverse direction, finer in the vicinity of the liquid/gas interface. The computational time step equals to 10^{-8} s. During the start-up, the plenum pressure drives the flow and the mass flux and the exit velocity of the jet increase with the plenum pressure. During the first 300 μs after the start of injection, jet velocity and orifice pressure difference increase from initial zero values to 200 m/s and 1.6 MPa, respectively. The maximum mass flux and pressure remain constant for 100 μs during the steady-state period. The air pressure in the gas chamber is 30 atm and the orifice diameter is 200 μm.

Fig. 8 illustrates the formation of a mushroom-shaped cap as the jet decelerates in the quiescent air along the chamber while the pressure drops and the jet exit velocity increases during the start of injection. The radial and axial scales are adjusted in each sub-figure to portray the relevant surface waves in a clear fashion. The mushroom-shaped cap grows in volume since the cap moves slower

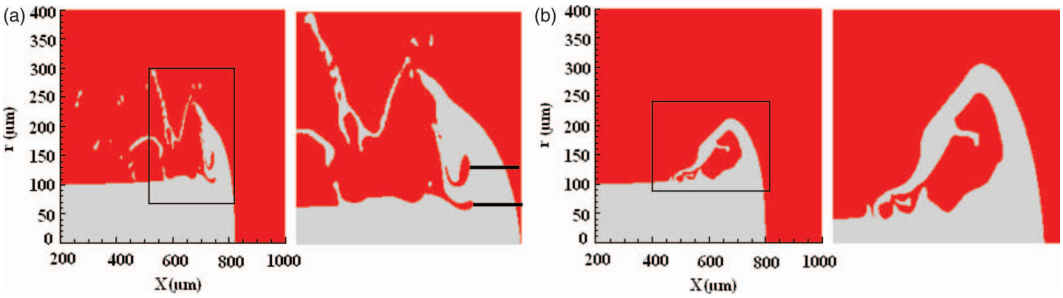

FIG. 8. Jet development, $\frac{\rho_g}{\rho_l} = 0.048$, $\Delta p_{max} = 1.6$ MPa, t = 40 μs (a) $Re = 16\,000$, $We = 230\,000$, (b) $Re = 16\,000$, $We = 23\,000$ (horizontal tick marks indicate secondary instability wavelength).

than the flow at the orifice exit. Strong vortices behind the cap roll back and entrain air into the rear side of the cap. These vortices and the shear stress at the liquid/gas interface are responsible for further instabilities that appear at the jet interface later in time. (The three-dimensional calculations of Shinjo and Umemura[2] indicated that the streamwise vortices join this strong vortex behind the cap and strong instabilities appear at the interface as well as the cap.[2]) The protrusions from the shear instability in the present axisymmetric simulations are actually cone-shaped liquid sheet structures in the streamwise direction. This behavior will be discussed for the three-dimensional liquid-segment model in Sec. VI.

The effects of surface tension on jet instability have been shown in Fig. 8(b). The surface tension coefficient in this figure is 10 times that of Fig. 8(a), keeping the *Re* equal to 16 000 for both cases. Clearly, by decreasing the surface tension, longer and thinner sheets form and small wavelengths appear at the rear side of the jet cap and strong KH and secondary instability waves appear on the liquid/gas interface. Thus, for this range of *Re* and *We*, small-scale wavelengths and protrusions become even smaller due to exposure to high local accelerations. Fig. 9(a) graphs the unstable structures at the jet interface at different sections of the jet at the same injection time, i.e., 100 μs for *Re* and *We* equal to 16 000 and 230 000, respectively. These three figures represent different regions of the jet in the axial direction, i.e., close to the orifice, middle section, and close to the head part of the jet, respectively. This figure indicates how different types of instabilities at the jet interface have been differentiated in this paper. The vertical tick marks show the KH wavelengths while the horizontal tick marks indicate shorter secondary wavelengths on top of the primary KH wavelengths, i.e., cones and also at the back of the jet cap.

The range of unstable KH and shorter secondary wavelengths during 100 μs from the start of injection has been demonstrated in Fig. 9(b). The first 10 μs is associated with the development and roll-up of the jet cap; that is, the upstream jet interface has not been distorted due to instabilities at this stage. After about 10 μs, the upstream interface starts to be distorted due to shear instability and wavelengths in the range of 60–120 μm appear at the interface. At 20 μs, secondary instability wavelengths (10–30 μm) were detected at the back of the jet cap. Simultaneously, KH waves continued to develop at the upstream interface further and air is entrained between the interfacial protrusions. As the liquid jet develops with time, drag causes the relative velocity between the liquid and air to decrease and, consequently, the primary KH wavelengths increase to more than 300 μm at 100 μs, greater than the diameter of the orifice. This is consistent with the linear KH theory; with negligible gravity, the decrease of the relative velocity between the liquid and gas causes an increase in the most unstable KH wavelength. The secondary wavelengths associated with these longer KH waves also increase to 40 μm at 100 μs compared to 10 to 30 μm secondary wavelengths observed at 20 μs. Therefore, there is a nonlinear interaction between the secondary instability that appears on wave crests with the shear or KH instability.

We expect acceleration of the surface to decrease as relative velocity decreases which would explain the increase in secondary wavelengths. The liquid jet builds momentum at the early stages of the injection while the pressure difference at the orifice increases. In addition, the drag forces acting on the liquid are also stronger at the beginning of the injection. This corresponds to higher

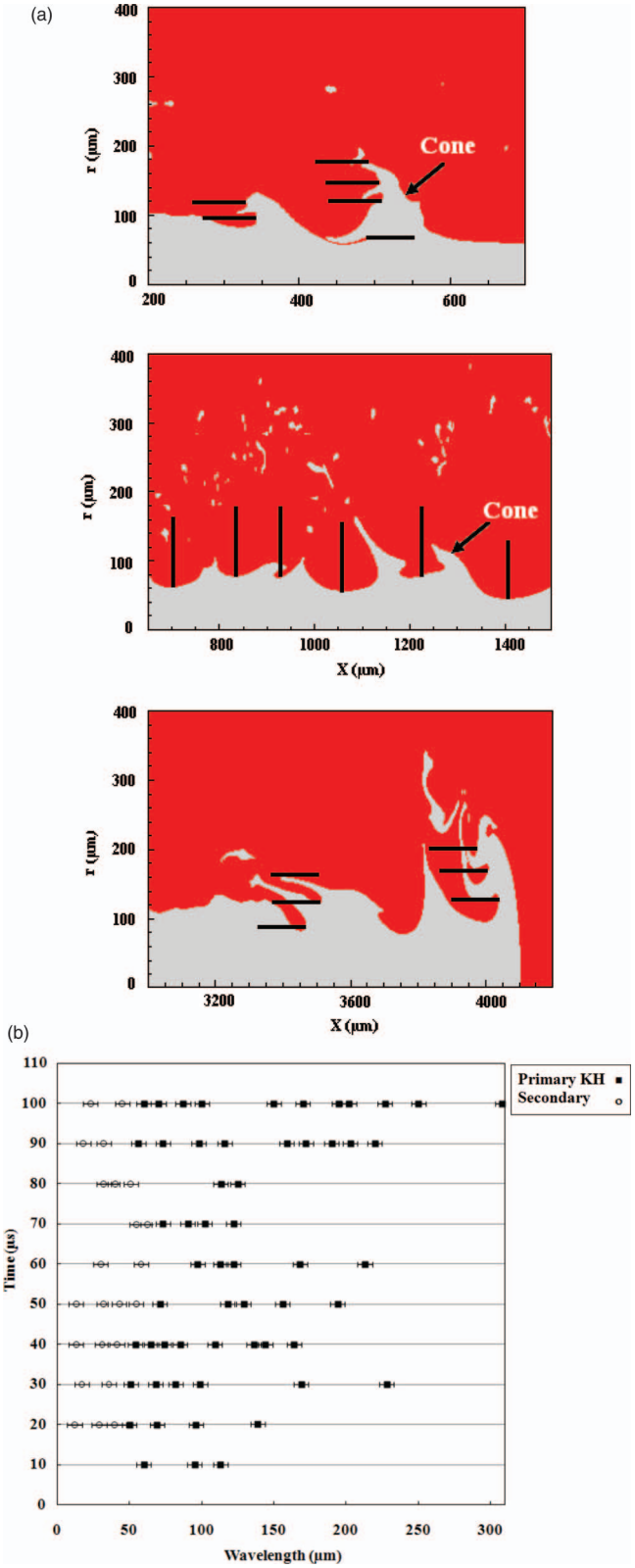

FIG. 9. (a) Unstable structures at the liquid interface at 100 μs indicating KH and secondary wavelengths at three regions: close to the orifice, middle section, and close to the head part of the jet (b) KH and secondary wavelength spectrum during start-up vs. time, the error bars correspond to 5 μm ($\frac{\rho_g}{\rho_l} = 0.048$, $\Delta p_{max} = 1.6$ MPa, $Re = 16\,000$, $We = 230\,000$).

jet acceleration and high shear stress at the liquid/gas interface leading to small wavelength KH and secondary instabilities. As the jet develops, the acceleration of the liquid jet and the drag forces decrease; thus, longer wavelengths appear at the interface. Secondary instability with smaller wavelengths compared to KH waves, first appear on the back of the jet cap and later at the interface. In addition, it can be concluded from this picture that the deformation of the jet starts from the head part and is convected up-stream toward the orifice. This transmission of the disturbances from the jet tip in the opposite direction of the liquid jet flow has also been indicated by Shinjo and Umemura.[2]

The axisymmetric secondary instability that follows the KH instability develops after 40 μs. In Sec. VI, it shall be seen from three-dimensional computations that azimuthal instability occurs in a shorter time. Thus, after a certain time period, the details of the hydrodynamic instability given by an axisymmetric instability are not practical. However, certain gross features can still be estimated such as potential lengths and decelerations.

It is instructive to investigate the spatial variation of velocity for liquid points located on the jet axis during the start-up period. The simulations show that the jet centerline velocity decreases in the axial direction due to the drag forces acting on the bulk accumulated liquid on the jet cap. The ratio of the jet tip velocity to orifice exit velocity at 100 μs is lower for lower *Re*. The high *Re* jet accelerates to higher velocity at the orifice exit and travels further downstream at comparable instants of time. The effects of drag forces are not dominant in the downstream direction for high *Re*. In other words, we can approximate that the liquid on the centerline of the jet initially has the same acceleration as the jet injection at the nozzle exit. This essentially portrays any element of mass as a ballistic slug of liquid following a constant velocity with time, i.e., the Lagrangian time derivative of velocity is zero although velocity spatially varies in the downstream direction. Thus, for larger *Re*, instead of simulating the full jet, streamwise segments of the jet will be considered as ballistic slugs coming from the orifice. This model will be discussed in Sec. V. More details about the full jet simulations are provided in Jarrahbashi[57] and Appendix A.

V. AXISYMMETRIC LIQUID-SEGMENT MODEL

The full jet instability discussed earlier originates at a certain point and develops in space, in the direction of mean velocity, i.e., spatial instability. The initial stages of jet development, i.e., the formation of jet cap and the convection of the instabilities upstream can be captured with sufficient resolution as discussed in Secs. II and IV. However, numerical modeling of the problem later in time requires much longer computational domains to allow the spatial development of the flow. We now simplify that computational challenge by examining only a segment of the mass in the jet. The jet instability problem simulated in the laboratory frame is now transferred to a new accelerating coordinate system consistent with the acceleration of the liquid on the centerline obtained in the full transient jet simulation. The gas accelerates over the initially stagnant liquid and the generated instabilities at the interface will develop temporally. Since the temporal instability dominates in this model, most comparisons with a full jet reported here, especially the frequency and amplification rate of the instabilities, are mainly qualitative. However, as will be illustrated, the KH and secondary wavelengths will be in the same range as for the full transient jet.

A small segment of the jet, e.g., 1 mm in length with a 200-μm radius surrounded by air at 30 atm is considered. The liquid is initially quiescent while the gas blows over the liquid from right to left. The gas initial velocity is consistent with the maximum velocity of the jet in the laboratory frame when its penetration length is 1 mm. The computational domain and boundary conditions were described in Sec. III. The fluid properties are based on the initial monotonic velocity profile which has a very thin boundary layer for the liquid with velocity varying between zero to 70 m/s along the 100-μm orifice radius combined with a thick boundary layer for the gas varying between 70 and 100 m/s along 300 μm in radial direction. As discussed for the full jet simulation, during the first stages of jet penetration (e.g., X = 5D), initial interfacial wavelengths about 100 μm appear as a result of shear instability. Therefore, in the liquid-segment model initial disturbances of length 100 μm have been applied on the liquid/gas interface simulating the effects of shear instability.

Fig. 10 illustrates the development of the unstable wavelengths at the liquid/gas interface. The primary shear instability waves, i.e., KH waves with wavelengths of 100–200 μm, travel upstream

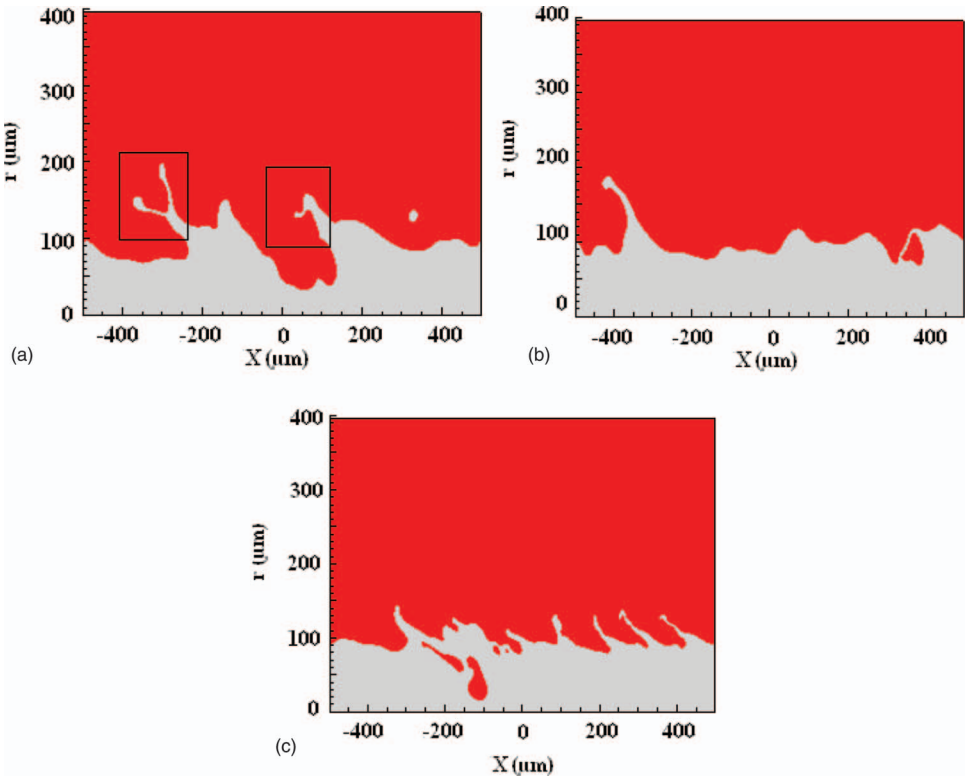

FIG. 10. Instabilities at the liquid/gas interface for liquid-segment model at $t = 30$ μs, (a) $Re = 16\,000$, $We = 23\,000$, $a = 800\,000$ m/s^2 and (b) $Re = 16\,000$, $We = 23\,000$, $a = 400\,000$ m/s^2, and (c) $Re = 16\,000$, $We = 230\,000$, $a = 800\,000$ m/s^2.

relative to the liquid (leftwards) while their amplitude increases and the liquid crests are drawn into cone shapes. These crests turn and roll-up in the flow direction (right to left.) In addition to the acceleration of the frame of reference, these crests are exposed to very high local accelerations normal to their interface that subject them to small-scale secondary instabilities; these small-scale secondary instabilities appear at the edge of the crests. At this stage, surface tension is the dominant effect in determining the size of the rings detached from the tip of these wavy liquid sheets. The axisymmetric detachment will be shown to be not physically authentic because azimuthal instabilities will occur earlier.

As is shown in Fig. 10, some of the cone protrusions turn into a very thin film with a small neck and a blob of liquid at their end part. The primary instability at the interface experiences two effects. First, the surface waves convect downstream (from right to left) in the flow direction along the section, i.e., an indication of an orientation effect. A pressure gradient in the axial direction is allowed by the boundary condition as specified in Sec. III to represent the accelerating jet. So, an element of spatial instability is added to the temporal behavior. Second, while convecting upstream, their amplitude grows, secondary instability develops and a blob of liquid appears at their ends. Therefore, at 30 μs, some of the cones have developed the secondary instability at their edge and a blob of liquid is observed at their end. However, other cones reach a greater length, i.e., amplified amplitude, before the secondary instability appears at their interface. Therefore, in these pictures, a few of the cones have been shown with the blob. Other cones will experience the same effect later in time but are not shown in this picture. Capturing these small capillary waves and the bulk liquid volume at the tip of the cones supports the claim that grid resolution is sufficient to explain the dynamics. In addition, three-dimensional analysis of ligament formation that will be discussed in Sec. VI confirms a similar phenomenon as observed in this axisymmetric simulation except, of course, it becomes three-dimensional. Development of both KH and secondary instabilities on the cones for the liquid-segment model repeats the same phenomena observed for full jet. Therefore, the liquid-segment describes the behavior of the liquid jet at the stage where instabilities have been conveyed upstream (toward the orifice exit) rather than concentrated at the jet head.

Fig. 10(b) illustrates the instabilities due to an acceleration half of that of Fig. 10(a) at 30 μs after the start of injection while other parameters, i.e., *Re* and *We*, remain constant. Higher acceleration of the frame of reference is equivalent to shorter start-up period for constant maximum liquid jet exit velocity. Higher acceleration enhances the growth rate of both temporal and spatial instability. In other words, increasing the acceleration of the frame of reference leads to the formation of longer (higher-amplitude) and thinner protrusions with smaller secondary wavelengths on their crests at comparable instants of time as a result of the secondary instability.

According to the viscous potential flow dispersion relation from Funada and Joseph,[27] at sub-millimeter, super-micrometer wavelength range of interest, surface tension has stabilizing effects for smaller wavelengths; thus, at higher *We*, smaller wavelengths are expected as discussed for full jet simulations. Fig. 10(c) shows the effects of a lower surface tension, i.e., one tenth that of Fig. 10(a), and for acceleration of the frame of reference equal to 800 000 m/s^2. A comparison depicts that, at a comparable instant of time, smaller waves and thinner cones appear at the liquid/gas interface for higher *We* with constant acceleration. More details about the axisymmetric liquid-segment calculations are provided in Appendix B.

VI. THREE-DIMENSIONAL LIQUID-SEGMENT MODEL

The three-dimensional liquid jet remains essentially axisymmetric in surface shape for early stages of injection and development, i.e., 30 μs for *Re* and *We* equal to 1600 and 230 000. So, for this period, the axisymmetric liquid-segment model is capable of describing the surface shape. However, three-dimensional vorticity fields and vortex structures have already began to form. Using a three-dimensional analysis of the liquid segment (versus the previous axisymmetric analysis) will allow investigation of the vorticity dynamics and its impact on three-dimensional instabilities that lead to the ligament formation and finally break-up. Comparison will be made with the vorticity dynamics of like-density jets, e.g., water into water and air jet into air.

The computational domain consists of a Cartesian grid. The liquid-segment with a circular cross sectional area, a length of 1 mm and a 200 μm diameter is consistent with the axisymmetric liquid-segment model and is centered in the computational domain in the *x*-direction as Fig. 11 depicts. High-pressure air blows over the liquid-segment that is initially stationary at the centerline. The initial velocity profile started from 70 m/s at the liquid/gas interface and increases to 100 m/s on the outer boundaries. The initial velocity of the liquid starts from zero on the centerline of the

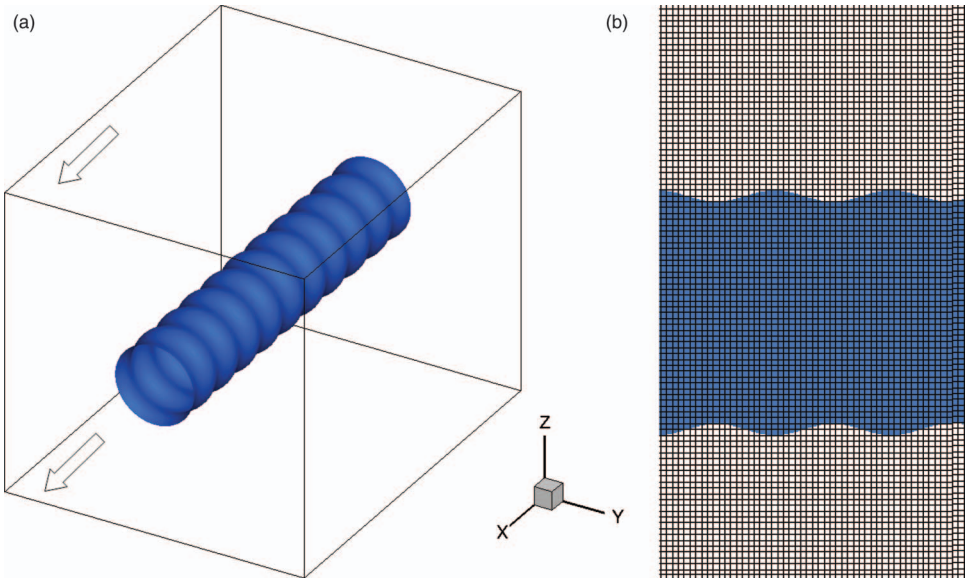

FIG. 11. (a) Computational domain including the liquid segment and initial disturbances at the interface; surrounding air blows in the positive *x*-direction as arrows indicate, (b) computational grid.

jet and exponentially increases to 70 m/s at the interface consistent with the axisymmetric liquid-segment model. Continuity of the velocity and shear stress has been applied across the interface and a pressure jump related to surface tension and local surface curvature has been considered. Navier-Stokes equations have been solved in three dimensions and the level-set method has been used to capture the interface topological changes.

The size of the computational domain in the y and z directions is 10 times that of the liquid jet diameter for the base calculations, more than 5×10^6 grid points with 5 μm uniform mesh-spacing has been used. A limited number of calculations have higher resolution. Periodic boundary conditions for all three components of velocity has been applied in the flow direction, zero normal gradients of velocity and pressure on the outer xz and xy planes have been applied. For the axisymmetric liquid-segment model discussed before, small initial disturbances of wavelength equal to 100 μm were applied at the interface. For the three-dimensional model, initial disturbances consist of a series of sinusoidal surface waves producing axisymmetric vortex rings 100 μm apart, aligned in the flow direction with a 10-μm initial amplitude. These vortex rings represent the initiation of primary shear or KH instability at the jet interface. The initial wavelength was chosen to be consistent with full-jet results.

A. Interface instability

The sequential development of the different instabilities at the interface of the liquid-segment at different instants of time is demonstrated in Figs. 12 and 13. Investigation of the topological changes at the interface shows that the initial vortex rings remain axisymmetric for some time after the start of computations and after cone-shaped structures form. Primary KH instability determines the distance between the crests of these cones. The secondary streamwise vorticity develops first in the braid regions, i.e., between the vortex rings, and ring regions similar to vortical structures observed in three-dimensional mixing layers.[39] The interaction of the streamwise vortex with the primary vortex rings leads to the distortion and stretch of the primary vortex rings at an angle with respect to the jet axis. In other words, the distortion of the vortex rings is associated with the formation of lobes on the conical-shaped crests at the liquid-gas interface. These lobes appear in Fig. 13 as a waviness in the azimuthal direction on the crests of the conical surface. This phenomenon of

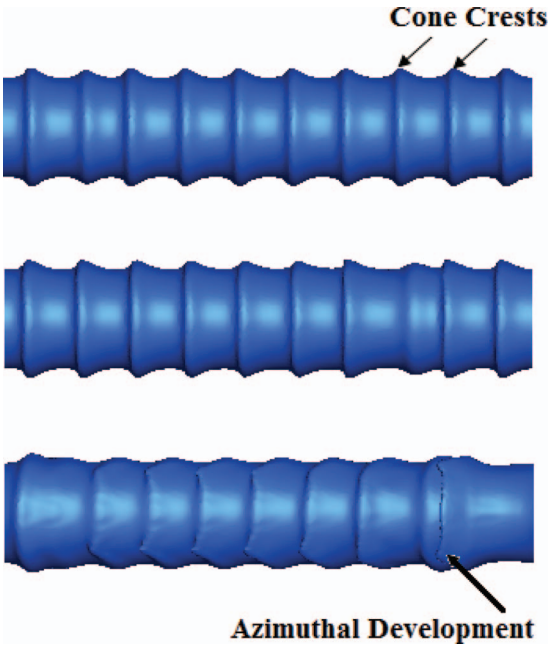

FIG. 12. (Top) t = 20 μs and (middle) t = 30 μs: instability remains axisymmetric, (bottom) t = 40 μs: development of the cone-shaped structures, $\frac{\rho_g}{\rho_l} = 0.048$, $Re = 1600$, and $We = 230\,000$ (gas flows from right to left).

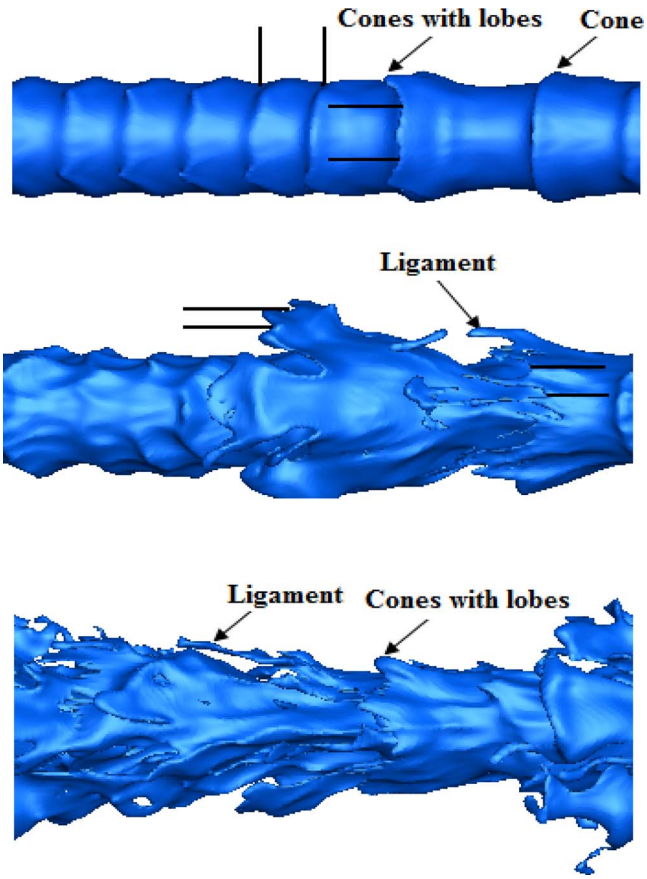

FIG. 13. (Top) t = 50 μs: development of the secondary transverse instability, (middle) t = 60 μs: formation of the ligaments from the transverse instability, (bottom) t = 70 μs: elongation of the ligaments, $\frac{\rho_g}{\rho_l} = 0.048$, $Re = 1600$, and $We = 230\,000$ (gas flows from right to left).

vortex ring distortion has been observed experimentally for like-density round liquid jet (without an interface) by Liepmann and Gharib[38] and numerically by Brancher, Chomaz, and Huerre[44] for three-dimensional round jets subjected to streamwise and azimuthal perturbations. Related vorticity dynamics will be discussed later in this section.

Fig. 13 shows the formation of smaller wavelengths in the azimuthal direction indicated with horizontal tick marks. The primary KH wavelengths, on the other hand, are shown with vertical tick marks. These azimuthal protrusions are drawn from the cone-shaped structures and produce the ligaments that grow in lengths later. The cross-sectional area of the ligament decreases near its tip and droplets will break-off from the liquid jet due to capillary effects. The KH wavelengths vary between 100 and 150 μm. The measured transverse wavelengths varies between 20 and 70 μm. Wavelengths on the ligaments vary between 15 and 40 μm. Therefore, wavelengths at the edge of the ligaments are smaller than those of the transverse instability. The ranges of both KH and transverse instability wavelengths are consistent with the range of wavelengths observed for the axisymmetric liquid-segment model. Consequently, the range of measured wavelengths have been correctly predicted by the previously discussed axisymmetric model although there are differences in their physics.

Fig. 14 depicts axisymmetric liquid-segment simulations for the same *Re* and *We* conditions as discussed above for three-dimensional liquid-segment model. The cone-shape structures are shown in this figure. At t = 30 μs, the primary instability is developing and the crests of the cone are stretching consistently with the three-dimensional segment analysis. However, in the three-dimensional model, azimuthal instability and formation of the lobes have occurred at t = 30 μs as shown in Fig. 12.

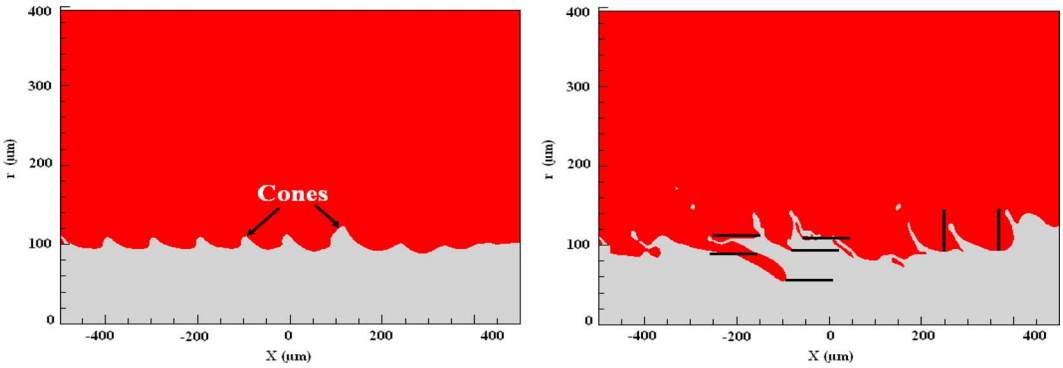

FIG. 14. (Left) t = 30 μs: formation of cone-shaped structures, (right) t = 60 μs: development of the cone-shaped structures and appearance of secondary instability on the backside of the cones for axisymmetric liquid-segment model, $\frac{\rho_g}{\rho_l} = 0.048$, $Re = 1600$, and $We = 230\,000$ (gas flows from right to left.)

At t = 60 μs, secondary axisymmetric instability wavelengths have grown on the cones as the horizontal tick marks in Fig. 14 indicate and ligaments have been formed from the secondary instability in the axisymmetric model. The vertical tick marks illustrate the primary KH instability wavelength, i.e., the distance between the cones. It can be deduced from Fig. 14 that, in the earliest stage, both axisymmetric and three-dimensional models follow the same mechanism of formation of the primary KH instability, i.e., axisymmetric cone-shape structures are formed. However, the secondary instabilities, which are of similar wavelengths, develop more slowly in the axisymmetric liquid-segment compared to the three-dimensional model. So, in the three-dimensional realization, the secondary axisymmetric instability appears to be irrelevant because it does not appear while axisymmetric behavior still exists.

Fig. 15 schematically shows the formation of the ligaments from the lobes on the cone-shaped structures. The ligaments develop from the lobes due to the amplified secondary azimuthal instability in the transverse direction. These ligaments then stretch and small-scale instability appears at their interfaces. The overall instability mechanism of the liquid-segment is qualitatively similar to the experiments of Marmottant and Villermaux[1] shown in Fig. 1. Ligaments can form from simple stretching of the lobes. Ligaments can also be formed as a result of the perforation of the sheared surface of the lobes as shown in Fig. 16. As the lobe stretches into the gas flow, the thickness of the lobe decreases inside the lobe area; therefore, surface tension punctures the surface and a small hole appears on the lobe surface. At the onset of lobe perforation, the average lobe thickness for gas-to-liquid density ratio equal to 0.1, for dx = 5 μm was greater than 20 μm. So, clearly, the

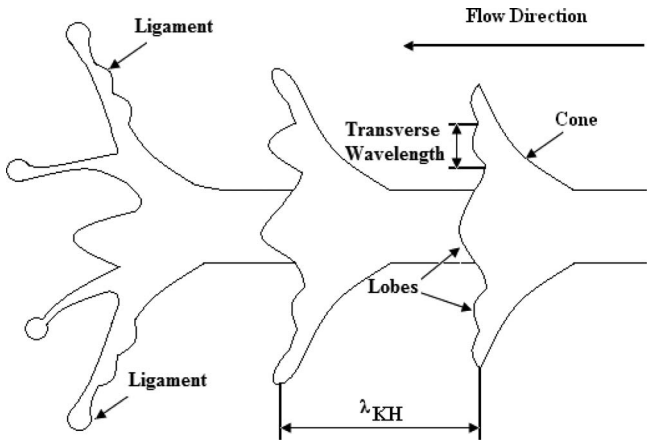

FIG. 15. Schematic of the secondary azimuthal instability in the transverse direction and formation of the ligaments.

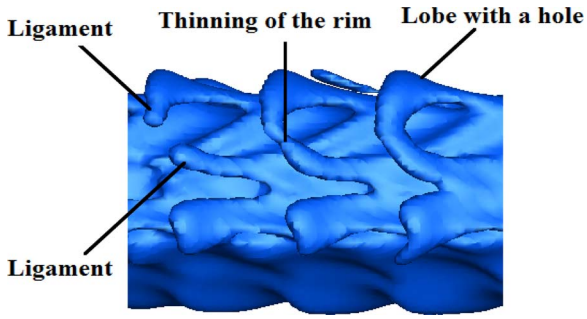

FIG. 16. Ligament production mechanism as a result of thinning and tearing of a lobe, $\frac{\rho_g}{\rho_l} = 0.5$, at t = 50 μs: $Re = 1600$ and $We = 230\,000$, $a = 800\,000$ m/s^2 (flow from right to left).

thickness of the lobe is larger than the artificial scales of the variable density region and perforation does not occur due to level-set calculations. In addition, with mesh refinement to 2.5 μm in all three-directions and reduction of fuzzy zone thickness by 50%, at comparable times the thickness of the lobes with a hole remains constant. Therefore, first, the lobe thickness in our numerical results is mesh independent. Second, the same mechanism created holes on the lobes at approximately the same locations with respect to the tip of the lobe. However, the holes appeared slightly earlier in time for refined mesh compared to previous coarse calculations. The hole expands later in time and its rims become thin enough to tear. Two ligaments appear as a result of tearing of this thin structure. Numerical simulations of Shinjo and Umemura[2] demonstrate the same phenomenon with lobe formation for a liquid jet injected into air. Thus, the same mechanism perforates the liquid sheets and produces ligaments. Note that tearing of planar sheets have been observed in experiment[58] and computation.[59]

We have observed both of these two mechanisms of ligament production, i.e., Figs. 15 and 16 in our simulations. However, for lower liquid-to-gas density ratios the first mechanism of lobe stretching dominates since the baroclinic effect, i.e., RT instability is an important factor to produce the transverse instability. Therefore, most of the ligaments appear as a result of the stretching of the small-wavelength transverse instabilities. In a private communication, Professor Villermaux has stated the lobe stretching is dominant compared to hole formation in his experiment for low gas-to-liquid density ratio. Our simulations indicate that for higher gas-to-liquid density ratios the second mechanism of ligament formation, i.e., from the tearing of the hole on the lobe dominates the first mechanism. The more likely appearance of hole formation on the lobes at high gas density is consistent with the findings of Rangel and Sirignano.[34] They predicted that the 2D dilatational mode of a combined KH-capillary instability for a thin liquid sheet became more probable as gas density increased. As already noted, it is likely that, when the lobe is stretched by the viscous action of the air stream, the lobe behaves similarly to a liquid bridge under tension and rupture becomes more probable. More study is required to explain fully the physics of the hole formation.

Effects of gas-to-liquid density ratio on the development of the instability at the jet interface has been shown in Figs. 17 and 18 at 50 and 80 μs, respectively. The gas density varies while the liquid density and other properties, e.g., *Re*, *We*, and the acceleration of the gas flow remain constant. At 50 μs, the lobes have been formed for all three cases; however, the lobes are more developed with a larger surface area for lower gas-to-liquid density ratio compared to higher density ratios. Therefore, as we approach like-density jets, i.e., higher gas-to-liquid density ratios, the deviation from axisymmetry is less evident at these earlier times although lobes have been formed in the transverse direction and the instability is three-dimensional.

If we define a non-dimensional time based on the gas viscosity and density as $t_{gg} = \frac{\mu_g t}{\rho_g D^2}$, where t_{gg} is the non-dimensional time, it is evident that the dimensional time varies proportional to the gas density assuming that other parameters are constant, i.e., $\frac{t_2}{t_1} \sim \frac{\rho_{g2}}{\rho_{g1}}$. Therefore, we expect the dimensional time for higher gas-to-liquid density ratio to be larger. Thus, the lower gas-to-liquid density ratio is more developed at comparable dimensional time, i.e., 50 μs. The discrepancies

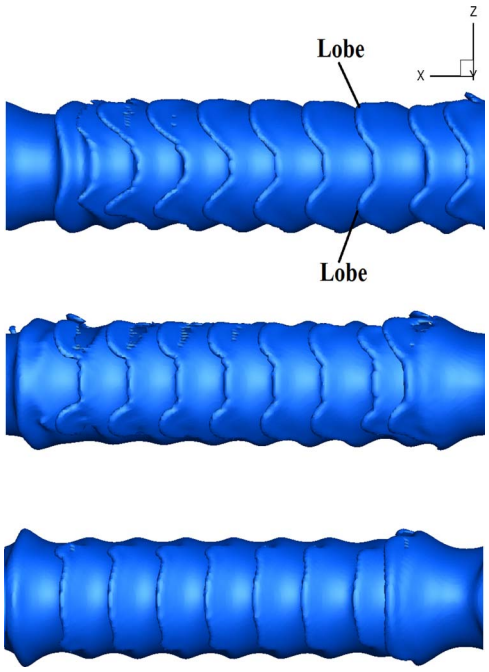

FIG. 17. Effects of gas-to-liquid density ratio on the development of the secondary transverse instability, (top) $\frac{\rho_g}{\rho_l} = 0.1$, (middle) $\frac{\rho_g}{\rho_l} = 0.5$, (bottom) $\frac{\rho_g}{\rho_l} = 0.9$, at t = 50 μs: $Re = 1600$ and $We = 230\,000$, $a = 800\,000$ m/s^2 (gas flows from right to left).

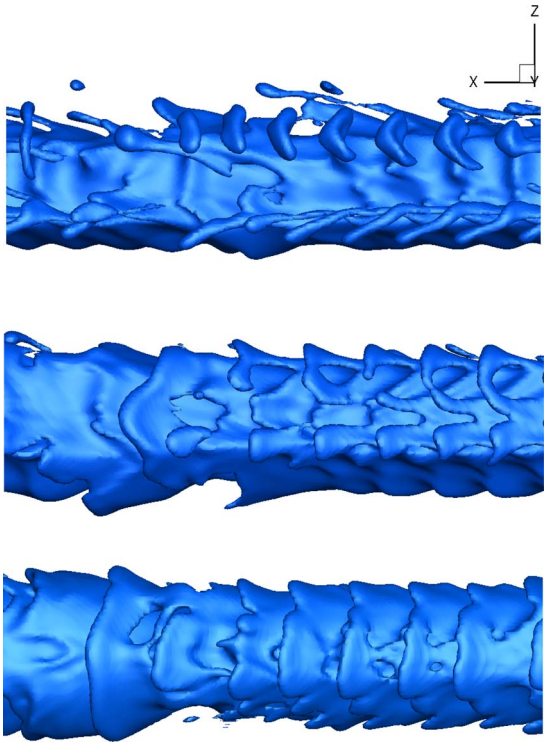

FIG. 18. Effects of gas-to-liquid density ratio on the development of the secondary transverse instability, (top) $\frac{\rho_g}{\rho_l} = 0.1$, (middle) $\frac{\rho_g}{\rho_l} = 0.5$, (bottom) $\frac{\rho_g}{\rho_l} = 0.9$, at t = 80 μs: $Re = 1600$ and $We = 230\,000$, $a = 800\,000$ m/s^2 (gas flows from right to left).

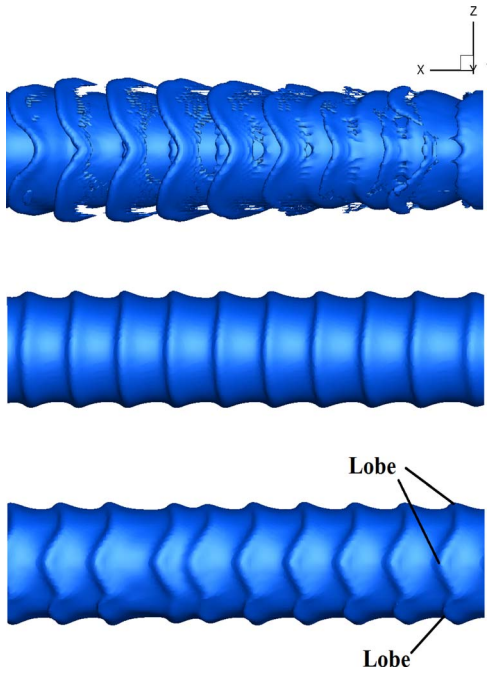

FIG. 19. Effects of surface tension and liquid viscosity on the development of the secondary transverse instability for $\frac{\rho_g}{\rho_l} = 0.1$, (top) $Re = 1600$, $We = 6.5 \times 10^9$ at t = 50 μs (middle) $Re = 16\,000$, $We = 230\,000$ at t = 50 μs, (bottom) $Re = 16\,000$, $We = 230\,000$ at t = 80 μs ($a = 800\,000$ m/s^2 for all cases; gas flows from right to left).

between these cases are more evident in Fig. 18 at 80 μs. Long and slender ligaments can be seen for lower density ratio; however, for higher density ratios the lobes are still developing. Small ligaments have been formed based on the hole-tearing mechanism discussed in Fig. 16.

Fig. 19 (top) demonstrates the effects of a very small surface tension coefficient on the interface instability for $\frac{\rho_g}{\rho_l} = 0.1$ compared to Fig. 17 (top) at 50 μs with same acceleration and *Re*. This figure indicates the role of the surface tension on the perforation of the lobes. The lobes have been perforated drastically for higher *We*. Fig. 19 (middle and bottom) shows the development of the instability for lower liquid viscosity, i.e., higher *Re* for same gas-to-liquid density ratio at 50 μs and 80 μs compared to Figs. 17 and 18 (top). The *We*, acceleration, and fluid inertia are the same. Referring to the same non-dimensional time discussed earlier, this time based on the liquid properties, i.e., $t_{ll} = \frac{\mu_l t}{\rho_l D^2}$, the dimensional time is inversely proportional to the liquid viscosity: $\frac{t_2}{t_1} \sim \frac{\mu_{l1}}{\mu_{l2}}$. These figures indicate that the transverse instability develops later for lower liquid viscosity. The lobes have not been formed at 50 μs and the flow is nearly axisymmetric. It has been shown in the literature that the number of the lobes (streamwise vorticity structures), i.e., mode number of azimuthal instability, increases with *Re* for homogenous jet flow.[38] This behavior is similar to non-homogenous jet flows. As shown in Fig. 19 (bottom), three of the total five lobes can be seen in the perspective from the *y* direction at 80 μs compared to the four lobes shown in Fig. 17 (top) for lower *Re*. Experiments of Liepmann and Gharib[38] showed that for a homogenous jet flow *Re* less than 5000 based on the jet exit velocity the azimuthal mode number varied between five and six. Fig. 17 shows that for non-perturbed flow conditions the natural azimuthal mode number equal to four is triggered at lower *Re*. However, by increasing *Re* other mode numbers will evolve. These results confirm that numerical errors do not force the instability mechanism toward mode number equal to four. Error is expected to increase with increasing Reynolds number. For $Re = 1600$, four lobes are a natural consequence. Effects of other initial conditions on the development of different azimuthal wave numbers will be discussed in Sec. VI C. The combined results indicate that the non-dimensional time should be defined based on liquid viscosity and gas density. That is, $t_{lg} = \frac{\mu_l t}{\rho_g D^2}$. We are capable of predicting the dimensional time at which certain flow instabilities, e.g., lobe formations, occur at

the interface for different gas densities. However, at the same non-dimensional time, the interface of two cases with different gas densities is not exactly the same since there are other factors involved in predicting the interface shape, e.g., the gas boundary layer thickness.

B. Vorticity dynamics

In this section, the interface instabilities observed in Sec. VI A will be explained based on the vorticity dynamics of the flow. As mentioned earlier, the initial axisymmetric instability consisted of a series of vortex rings in the streamwise direction. Azimuthal instability propagates around the vortex ring producing a waviness and distortion on their structure. We will show that streamwise vortices will form causing more deviation from the axisymmetry and the interaction of the streamwise vortex with the primary vortex rings leads to the distortion and stretch of the primary vortex rings at an angle with respect to the jet axis.

The streamwise vortices are actually pairs of counter-rotating vortices for like-density jets.[38,44] Figs. 20 and 21 show the streamwise vorticity contours and the location of the liquid-jet interface for density ratio equal to 0.1 at 20 μs in the xz and xy planes, respectively. Fig. 20 demonstrates the streamwise vorticity contours at two locations; first, crossing the center of the jet, i.e., $y = 0$ and second, very close to the liquid-jet interface, i.e., $y = R$, where R is the liquid jet radius. The slices AA and BB indicate a braid and the adjacent ring. The gray and black colors represent the positive and negative band of values, respectively. Counter-rotating vortex pairs in the streamwise direction can be seen in both the ring and braid regions. This figure also shows that the streamwise vorticity originates in the braid region, i.e., the black streamwise vortex from slice AA is wrapped around the ring shown in slice BB. It has been shown in Fig. 4 that the streamwise vorticity from the braid region has been wrapped around the ring in like-density jets.[38] Fig. 20 also shows that due to the formation of streamwise vortices, the vorticity structure is not symmetric with respect to the

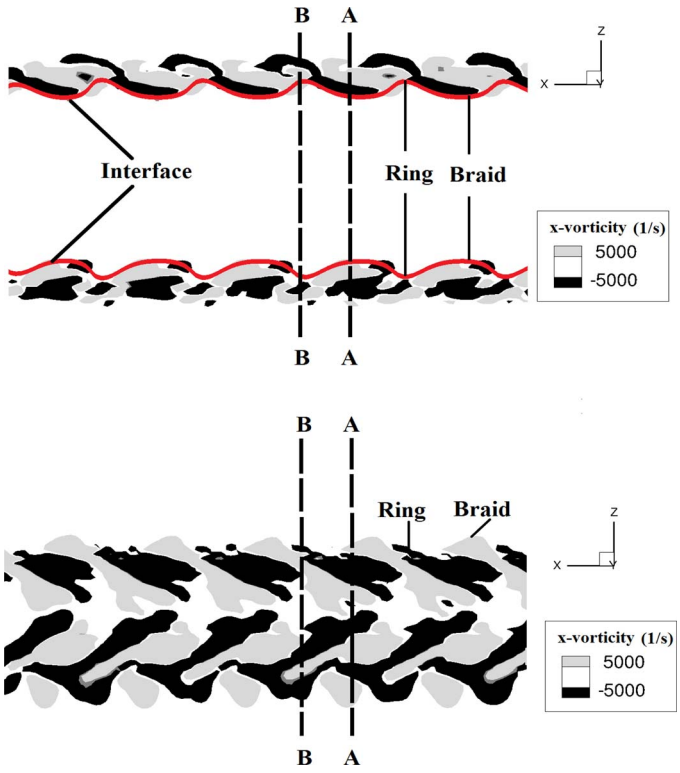

FIG. 20. Streamwise counter-rotating vortex pairs in xz plane at t = 20 μs, $Re = 1600$, $We = 230\,000$, $\frac{\rho_g}{\rho_l} = 0.1$, $a = 800\,000$ m/s^2, (top) $y = 0$ meridian plane and (bottom) $y = R$ plane (gas flows from right to left).

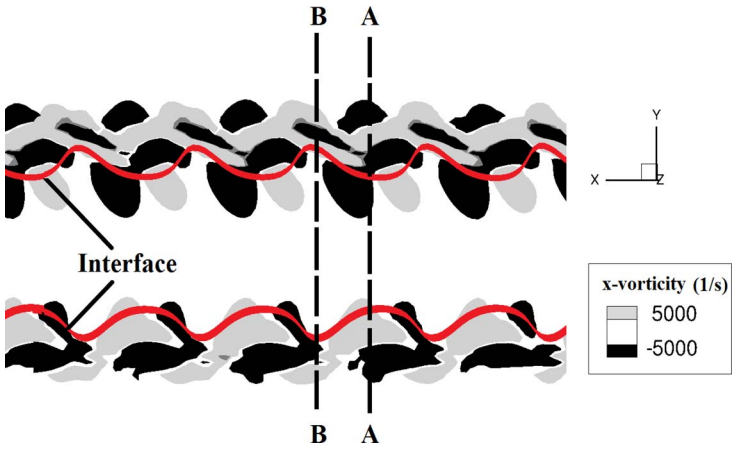

FIG. 21. Streamwise counter-rotating vortex pairs in xy plane at $z = 0$ and t = 20 μs, $Re = 1600$, $We = 230\,000$, $\frac{\rho_g}{\rho_l} = 0.1$, $a = 800\,000$ m/s^2 (gas flows from right to left).

xy plane. The contours of the streamwise vorticity in the plane at $y = R$, i.e., at the bottom of Fig. 20 indicates the positive and negative streamwise vortex pairs alternate in the streamwise direction and the vorticity structures have been wrapped around each other.

Fig. 21 shows that the structure of streamwise vorticity is similar to the hairpin vortex structure that has been observed in three-dimensional mixing layers. A magnified picture of the streamwise vorticity contours in Fig. 20 is shown in Fig. 22. The circles indicate the location of the vortex rings. The pairs of streamwise vortex structures envelop the ring similar to the situation observed in three-dimensional mixing layer as was shown in Fig. 6. A cross-sectional view of Fig. 6 represents the vortex rings with streamwise vortex structures with different signs on top and bellow the primary vortex rings. These structures connect two adjacent vortex rings by warping around them.

Fig. 23 demonstrates the streamwise vorticity contours at slices AA and BB of Fig. 20 in the yz plane that show a braid (AA) and its adjacent ring (BB) at 20 μs. Pairs of streamwise vorticity, alternately positive (gray) and negative (black) values, can be seen around the liquid jet in both braid and ring regions. The major difference between the streamwise vortex structures in the braid and ring is the reversed sign of the vorticity at the same azimuthal location on the yz plane. This sign change is due to the fact that the vorticity in the ring is actually originating from the upstream braid adjacent to the ring as was shown in Fig. 20. Brancher, Chomaz, and Huerre[44] indicated that the distribution of streamwise vorticity in the ring region displays a 180° shift with respect to that of the braid region for homogenous jet flow. Simulations of Danaila, Dusek, and Anselmet[45] show the

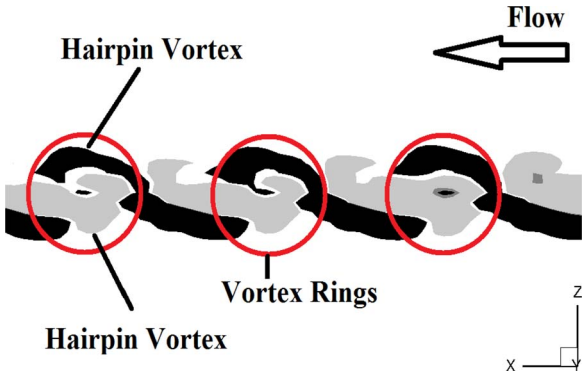

FIG. 22. Streamwise vorticity contours wrapping around the ring at t = 20 μs showing hairpin vortex structures, $Re = 1600$, $We = 230\,000$, $\frac{\rho_g}{\rho_l} = 0.1$, $a = 800\,000$ m/s^2.

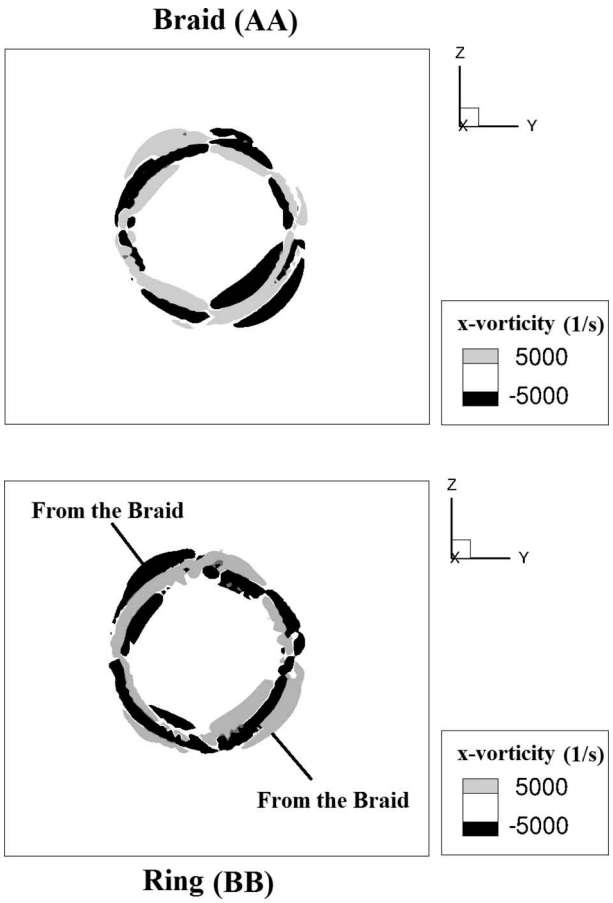

FIG. 23. Azimuthal distribution of streamwise vorticity contours in the braid and ring regions in the yz plane at t = 20 μs, $Re = 1600$, $We = 230\,000$, $\frac{\rho_g}{\rho_l} = 0.1$, $a = 800\,000$ m/s^2.

same distribution of streamwise vorticity in the braid and ring region for like-density jets. Therefore, this is the prevailing trend in non-homogenous jet flow as well as like-density jets.

Figs. 24 and 27 show the development of the instability on the liquid jet as well as the vorticity vector projection on the liquid-gas interface for 10–60 μs after the start of simulations. Note that the locations of the crests are not constant with time since the instability develops spatially and temporally in the liquid segment. The vorticity vectors are primarily circular at 10 μs representing the axisymmetric behavior of the jet at that time. Streamwise component of vorticity form in the braid region at 20 μs; however, vortex lines remain nearly circular in the ring region as shown in Fig. 24. Therefore, streamwise vortices originate in the braid first. Experimental results for both like-density jets and three-dimensional mixing layers[38,39] indicate the same behavior. It is also evident from this figure that the streamwise vorticity changes sign in the braid region, i.e., forming counter-rotating pairs in the streamwise direction. Note that two-dimensional "sink points" appear in the projections of Fig. 24 at 20 μs; however, vorticity is divergence free in three dimensions. So, a 2D sink implies a strong turning of the vorticity vector in the third dimension.

Fig. 25(a) demonstrates the distortion of the vortex lines in the braid region in the yz plane at 20 μs. Instabilities on the vortex lines are shown with four arrows at 90° intervals around the liquid jet that is shown in gray color. The vortex lines inside the liquid remain approximately circular; however, the vortex lines produce four hairpin vortices close to the liquid-gas interface, i.e., the instability mode number is equal to four consistent with the mode number observed by Danaila, Dusek, and Anselmet[45] for their unforced simulation, i.e., "natural mode" for homogenous jet flows. In addition, the spatial location of pairs of streamwise vorticity in the braid region, i.e., the hairpin

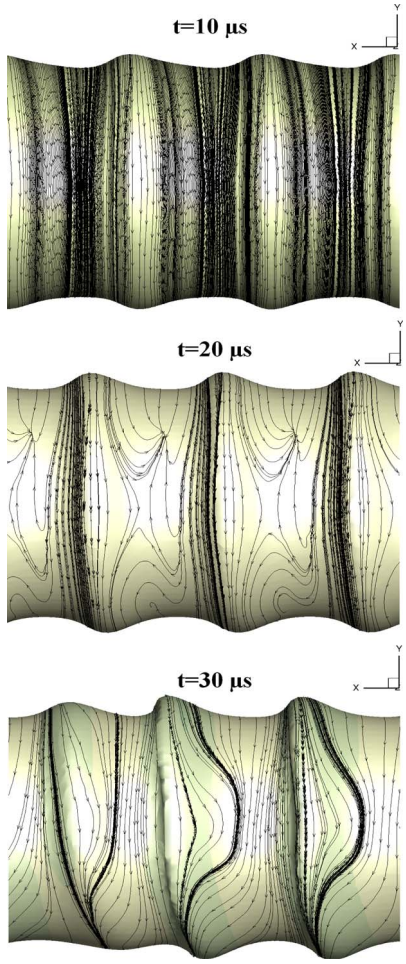

FIG. 24. Vorticity vectors projected on the liquid-gas interface at t = 10, 20, and 30 μs in perspective from z direction, $Re = 1600$, $We = 230\,000$, $\frac{\rho_g}{\rho_l} = 0.1$, $a = 800\,000$ m/s^2 (gas flows from right to left).

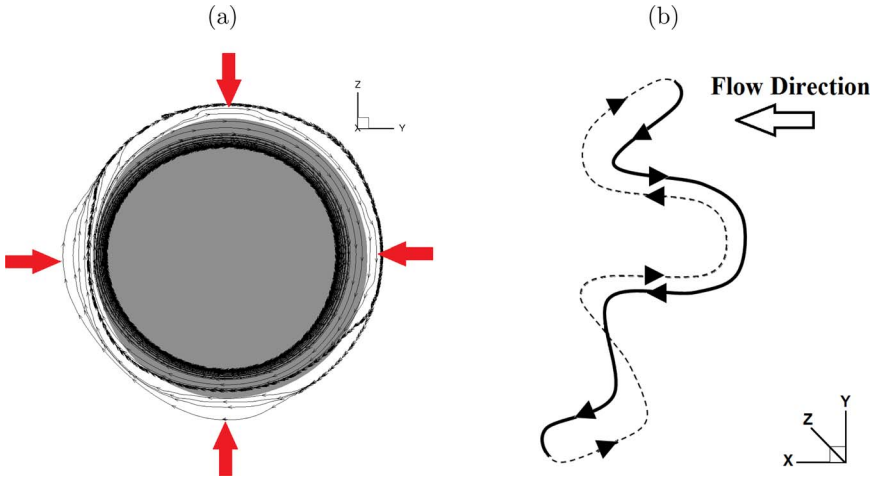

FIG. 25. (a) Instabilities on the vortex lines in the braid region in the yz plane showing four hairpin vortices at 90° intervals at t = 20 μs (flow is pointing outward and liquid phase is shown in gray). (b) A schematic of the distorted and tilted vortex line in the braid (the dashed line show the vortex line in the positive z-direction).

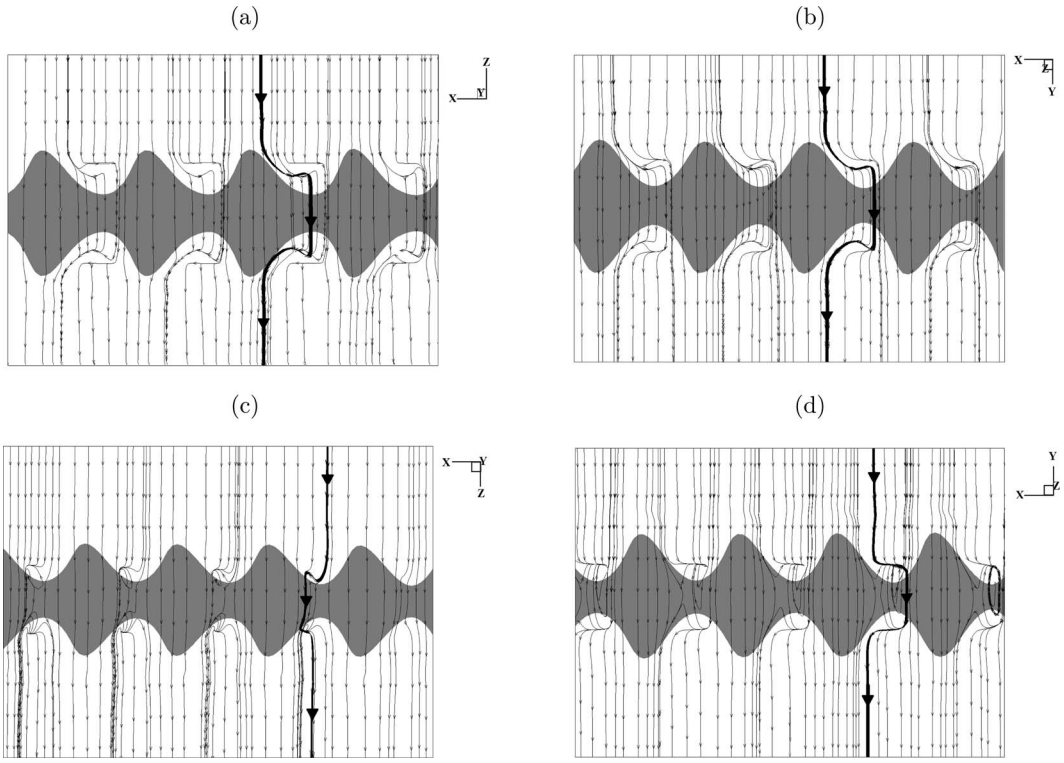

FIG. 26. Projected vortex lines on two-dimensional planes crossing the liquid-gas interface, 90° interval between the planes showing hairpin vortices in the braid at t = 20 μs, $Re = 1600$, $We = 230\,000$, $\frac{\rho_g}{\rho_l} = 0.1$, $a = 800\,000$ m/s^2: (a) xz plane $y > 0$, (b) xy plane $z > 0$, (c) xz plane $y < 0$, and (d) xy plane $z < 0$, (liquid phase is shown in gray and gas flows from right to left).

vortices in simulations performed by Danaila *et al.* in the plane perpendicular to the flow direction, is similar to that of Fig. 25(a). Figure 25(b) shows a schematic of the vortex line distortion in the braid. The vortex line tilts slightly with respect to the y-axis. In other words, the hairpin vortices are directing opposite to each other for positive and negative y values. This phenomenon is shown in Figs. 26(a)–26(d) that demonstrate the projection of the vortex lines on four planes around the liquid jet. Hairpin vortices are formed in the braid region pointing in the opposite direction of the flow except for Fig. 26(c) that the hairpin vortex is pointing in the flow direction. Also note that the vortex lines near the crests of the liquid are approximately straight. Therefore, the vorticity field becomes three-dimensional prior to 20 μs while the surface remain axisymmetric longer. Clearly, there is a time lag between the formation of the lobes on the cones and appearance of the counter-rotating vortex pairs in the braids.

As Fig. 24 indicates, at 30 μs, the vortex lines adjacent to the ring in the braid region bulge more in the negative x-direction consistent with the vortex structures discussed in Fig. 26. This deformation of vorticity occurs as a result of the interactions of the strains in the radial, azimuthal, and axial directions with the azimuthal and radial vorticity components that lead to the stretching and tilting of the vortex lines in the braids. A slight bulging can be seen at 20 μs; however, cone-shaped structures initiating at 30 μs intensify the strain rate in both braid and ring; thus, the vortex lines close to the ring curve even more. Note that the vortex lines in the ring are no longer axisymmetric and have tilted with respect to the y-axis. The vortex lines in the ring region will also produce four hairpin vortices corresponding to the locations in the transverse yz plane that produce four lobes on the crests of the liquid cone later in time, i.e., at 40 μs. However, as was indicated in Fig. 23, the streamwise vorticity in the ring region is 180° out of phase with respect to that of the braid region. Therefore, the hairpin vortices in the braid bulge in the opposite direction of the flow and tilt clockwise with respect to the y axis as was shown in Fig. 25(b). However, the hairpin vortices in the

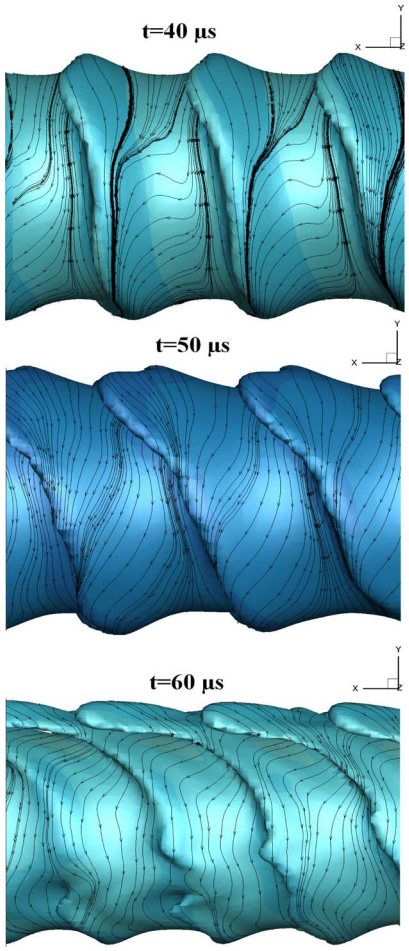

FIG. 27. Vorticity vectors projected on the liquid-gas interface at t = 40, 50, and 60 μs in perspective from z direction, $Re = 1600$, $We = 230\,000$, $\frac{\rho_g}{\rho_l} = 0.1$, $a = 800\,000$ m/s^2 (gas flows from right to left).

ring, i.e., lobes on the crest, form toward the flow direction, i.e., positive x-direction, and the ring tilts counter-clockwise with respect to the y axis. Tilting of the vortex rings in the flow direction has been observed in both simulations and experiments of homogenous jet flows.[45,60]

At 40 μs, the interface adjusts to the deformation of the vortex lines in the azimuthal direction and lobes have appeared around the crests as Figs. 27 and 28 represent. The vortex lines have a strong streamwise component in the braid region. The deformation of the vortex lines intensifies as the lobes on the crests grow and turn into slender ligaments as shown at 60 μs. The lobes appear with a 45°-phase difference in the yz plane with respect to the deformations shown in Fig. 25(a). Therefore, lobes can be seen better in a 90° rotation of the liquid jet with respect to the x-axis as illustrated in Fig. 28. Two of the four lobes of the crests are shown in this figure. The vortex lines on the lobes are slightly deformed at 40 μs; however, they bulge following the shape of the lobe at 50 μs as a result of the strain field-vorticity interaction producing a streamwise component of vorticity on the stretched surfaces of the lobes.

At 60 μs, the surface areas of the lobes have stretched and small holes have appeared close to the root of the lobe. The hole will expand later in time and produce new ligaments as discussed in Fig. 16. The average diameter of the holes at 60 μs is about 60 μm and there are at least 12 mesh points in each directions. Therefore, the present numerical simulation is capable of resolving these structures. Fig. 28 (bottom) demonstrates the turning of the vortex lines close to the tip of the lobes. This phenomenon is also shown in Fig. 29. The projected vortex lines on the lobe indicate hairpin vortices close to the tip of the lobe. Therefore, counter-rotating streamwise vortex pairs form as

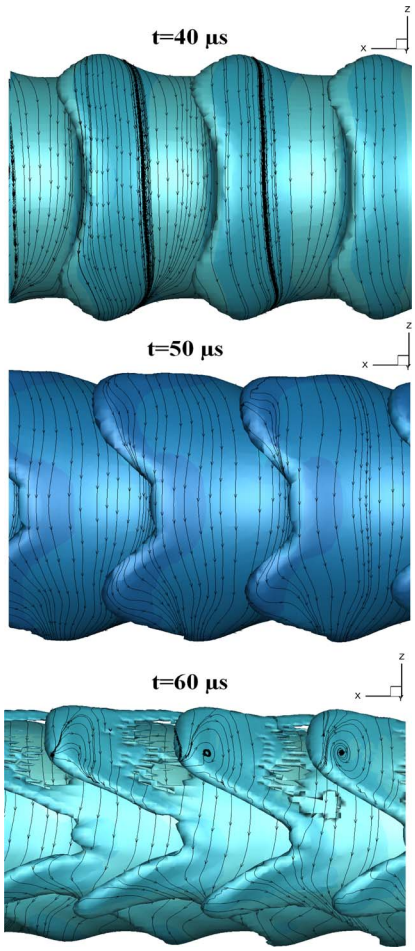

FIG. 28. Vorticity vectors projected on the liquid-gas interface at t = 40, 50, and 60 μs in perspective from y direction, $Re = 1600$, $We = 230\,000$, $\frac{\rho_g}{\rho_l} = 0.1$, $a = 800\,000$ m/s^2 (gas flows from right to left).

Fig. 29(a) shows. In addition, a sink point is formed near the tip of the lobe. This point indicates the existence of the vorticity component normal to this plane, i.e., in the yz plane.

The projections of the vorticity lines on yz and zx planes crossing the lobe near the sink point indicated by solid lines in Fig. 29(a) are shown in Figs. 29(b) and 29(c), respectively. The gray sections show the liquid phase. Fig. 29(b) demonstrates the hairpin vortices on the lobes around the crests with the turning of the vortex lines, i.e., y and z components of vorticity change sign along the hairpin vortex. The vortex lines far from the lobe remain axisymmetric. Note that the hairpin vortex around the lobe is located at a 45° position clockwise in the yz plane compared to the azimuthal distribution of the hairpin vortices in the braid shown in Fig. 25(a). The same orientation of the lobes in the transverse direction has been reported by Danaila, Dusek, and Anselmet[45] for homogenous jets. The sink point in this figure is also the projection of the vorticity component normal to this plane, i.e., x-direction that can be seen in Fig. 29(c).

As Fig. 29(c) shows, a strong streamwise vorticity forms in the positive x-direction and the vortex lines turn close to the tip of the lobe and produce the same hairpin vortices that were seen in Fig. 29(b). Therefore, the primary axisymmetric vortex rings transform into three-dimensional hairpin vortices that stretch in the streamwise-direction producing counter-rotating vortex pairs. Fig. 29(d) demonstrates the streamlines around the same lobe in the yz plane. The circulations shown on two sides of the lobe in the gas-phase indicate counter-rotating vortex pairs in the streamwise direction. The circulation on the right- and left-hand side of the lobe produces streamwise vorticity

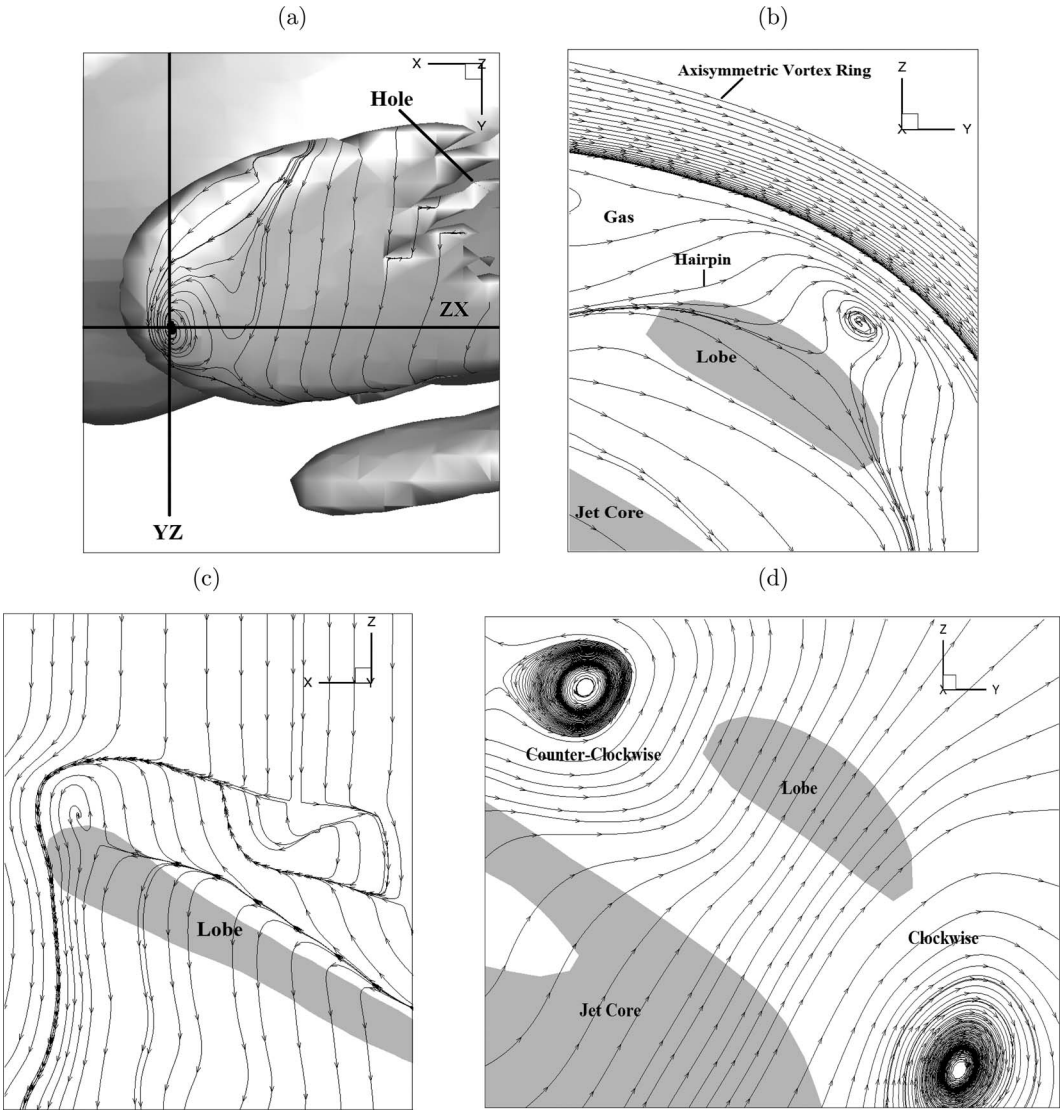

FIG. 29. Vorticity vectors projected on (a) the lobe, (b) the yz plane perpendicular to the lobe, (c) the zx plane perpendicular to the lobe, (d) streamlines in yz plane at t = 60 μs, $Re = 1600$, $We = 230\,000$, $\frac{\rho_g}{\rho_l} = 0.1$, $a = 800\,000$ m/s^2 (gray parts show the liquid phase).

pointing into and out of the plane, respectively. Therefore, the signs of the streamwise vorticity in the gas-phase are consistent with those of the liquid shown in Fig. 29(a).

Fig. 30(a) schematically shows the superposition of hairpin vortices forming from the primary circular vortex rings in the braid (solid line) and ring (dashed line) close to the liquid-gas interface. Four hairpin vortices have been shown here since four lobes initially appear around the jet as was discussed earlier. A 45° phase difference is evident between the azimuthal locations of the hairpin vortices in the braid and the ring. The vortex lines inside the liquid remain undisturbed. Fig. 30(b) shows a schematic of the three-dimensional distorted vortex ring on the cone and hairpin vortices stretched in the streamwise direction and tilted counter-clockwise with respect to the y-axis (compared with the vortex lines in the braid, i.e., Fig. 25(b)). Figs. 30(c) and 30(d) demonstrate a schematic of the stretched hairpin vortex and three different views of the same vortex in xy, yz, and zx planes, respectively. The solid circles here, i.e., sink points shown in Fig. 29, imply the existence of the vorticity component normal to that plane.

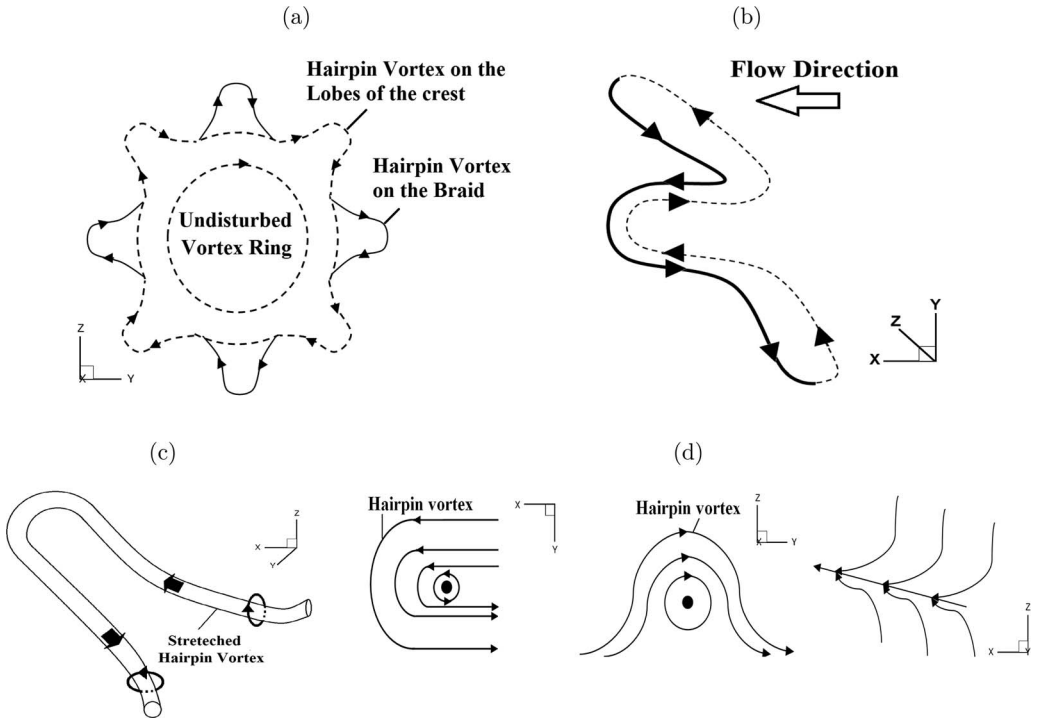

FIG. 30. Schematic of (a) superposition of distorted vortex lines in the braid (solid lines) and adjacent ring (dashed lines) showing the azimuthal location of hairpin vortices in the *yz* plane, (b) three-dimensional distorted vortex line on the cone crest (the dashed line shows the vortex line in the positive *z*-direction), (c) three-dimensional hairpin vortex, and (d) vorticity lines projected on two-dimensional planes on the cone.

Fig. 31 shows the streamlines in a section through two neighboring *yz* planes through the same cone at 50 μs where the darker part is the liquid surrounded by the gas. The flow is perpendicular to this plane pointing outward. At this stage, the cone has developed and its amplitude has increased. The axis of these vortex rings tilt with respect to the jet axis due to the amplification of the streamwise vorticity as was shown in Fig. 30(b). Therefore, if we show a plane perpendicular to the jet axis, we will observe two of the four lobes. The other two lobes can be detected by viewing another section perpendicular to the jet axis slightly away from the previous plane in the axial direction. Thus, the superposition of these two planes presented in Fig. 31 shows the four lobes formed on one cone. The central gray part is the core of the jet and the gray strips depict the intersection of the deformed cone with the plane. The combined figure demonstrates the formation of four counter-rotating vortices near the four lobes in the gas phase. Considering the streamlines in this figure, the signs of the vorticity on two sides of the lobe in the gas phase are consistent with the vorticity lines demonstrated on the liquid lobe in Fig. 29(a). For the counter-rotating vortex pairs in the gas phase, this situation is very similar to the streamwise vortices experimentally observed as side jets around the like-density jets[38] as was shown in Fig. 5. At each plane, a weak portion of the streamwise vortices from the other cone can be detected; however, the combined picture demonstrates the complete physics. The numerical simulations of Shinjo and Umemura[2] for non-homogenous jets showed that ligaments can be formed from the crests of the jet core due to the shear from local vortices. They also observed several small streamwise vortices at the liquid-gas interface; however, the detailed vortical motion that produced the ligaments was not discussed in their paper.

Liepmann and Gharib[38] suggested that most of the entrainment process occurs in the braid region while the liquid expels outward in the ring region to produce the side jets. Our simulations with non-homogenous jets shows the same phenomenon. Streamlines have been plotted in Fig. 32 for both ring and the adjacent braid region for density ratio equal to 0.1 at 20 μs. The flow generally points perpendicular to that plane out of the paper. The streamlines indicate inward radial motion

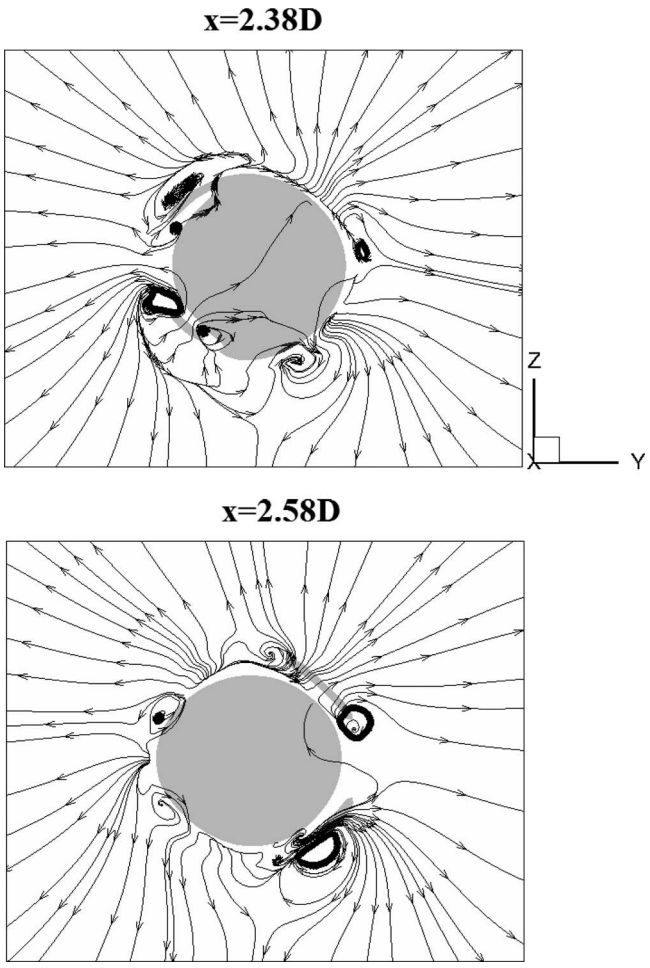

FIG. 31. Projected streamlines showing counter-rotating vortex pairs at the intersection of a cone with two consecutive yz planes, t = 50 μs, $Re = 1600$, $We = 230\,000$, $\frac{\rho_g}{\rho_l} = 0.1$, $a = 800\,000$ m/s^2 (liquid is shown in gray).

of the gas flow toward the center of the liquid jet in a region very close to the jet in the braid region and outward toward the gas phase in the ring region. In conclusion, there is an evident qualitative similarity between the homogenous jet flow and, over two orders of magnitude for density ratio, the non-homogenous jet flow.

C. Effects of initial conditions

The effects of initial non-axisymmetric perturbations of the ambient gas-phase velocity on the development of the instability on the liquid jet are shown in Fig. 33 at 20 and 60 μs . In particular, the initial axial velocity is now multiplied by the factor $1 + 0.01\sin(m\theta)$ where m and θ are azimuthal mode number and azimuthal angle, respectively. The initial KH surface wave amplitude is identical for all mode numbers. Three cases have been considered here: $m = 0$, i.e., axisymmetric, $m = 3$ and $m = 5$. As was discussed earlier, the mode number of the azimuthal Widnall instability on the vortex ring is consistent with the mode number of the non-axisymmetric perturbations for homogenous jet flow.[43] Three and five azimuthal wavelengths appear on the vortex rings initially for m equal to three and five, respectively. However, the cones are axisymmetric for the non-perturbed ($m = 0$) case at 20 μs as Fig. 33(a) shows. Therefore, there is a similarity between the Widnall azimuthal instability in homogenous and non-homogenous jet flows. For these small values of the initial perturbed velocity amplitude, the surface shape differs during the early period reflecting the

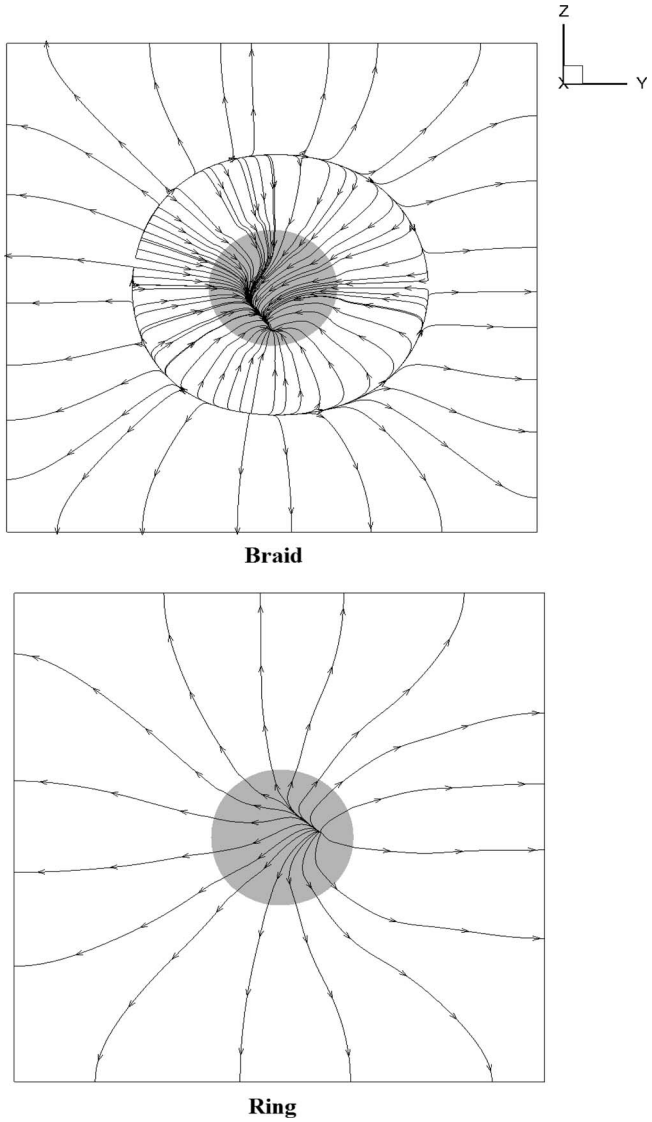

FIG. 32. Projected streamlines in the yz plane for the braid and ring regions at t = 20 μs, $Re = 1600$, $We = 230\,000$, $\frac{\rho_g}{\rho_l} = 0.1$, $a = 800\,000$ m/s^2.

initial perturbation; however, after 40 μs, the natural azimuthal instability with $m = 4$ dominates in all three cases. That is, four major lobes form on the cone crests and ligaments form as a result of the elongation of these lobes. Fig. 33(b) shows the surface instability at 60 μs for these three cases. Therefore, the interfaces are approximately similar eventually for both axisymmetric and non-axisymmetric initial conditions. Weak perturbation of the flow was made with $m = 4$ and a slight phase shift, i.e., the $1 + 0.05\sin(4\theta + \pi/8)$ factor was used. The results when compared to the unperturbed $m = 0$ case showed that, first, four lobes appeared in both cases; however, they appeared earlier in time for the perturbed case compared to the initially axisymmetric case, as was expected. Second, the orientation of the four lobes, after their development, differed in phase by $\pi/8$ between these two cases. This confirms that the natural mode does not have a fixed orientation related to numerical factors such as choice of grid and sweep direction.

Fig. 34(a) demonstrates a cross-section of the liquid jet (shown in gray) in the yz plane in the braid and adjacent ring for mode number equal to five at 10 μs. Here, the amplitude of the perturbation is increased from 0.01 to 0.1. As this figure shows, the interface has complied with the

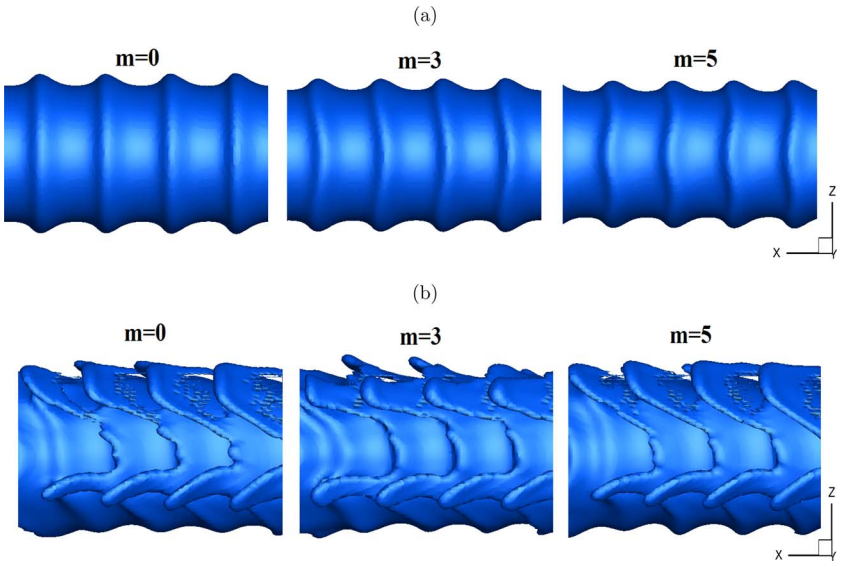

FIG. 33. Effects of perturbation mode on azimuthal Widnall instability on the vortex rings for mode numbers $m = 0$, $m = 3$, and $m = 5$ (a) 20 μs (b) 60 μs: initial velocity perturbation $1 + 0.01\sin(m\theta)$, $\frac{\rho_g}{\rho_l} = 0.1$, $Re = 1600$, $We = 230\,000$, $a = 800\,000$ m/s^2 (gas flows from right to left).

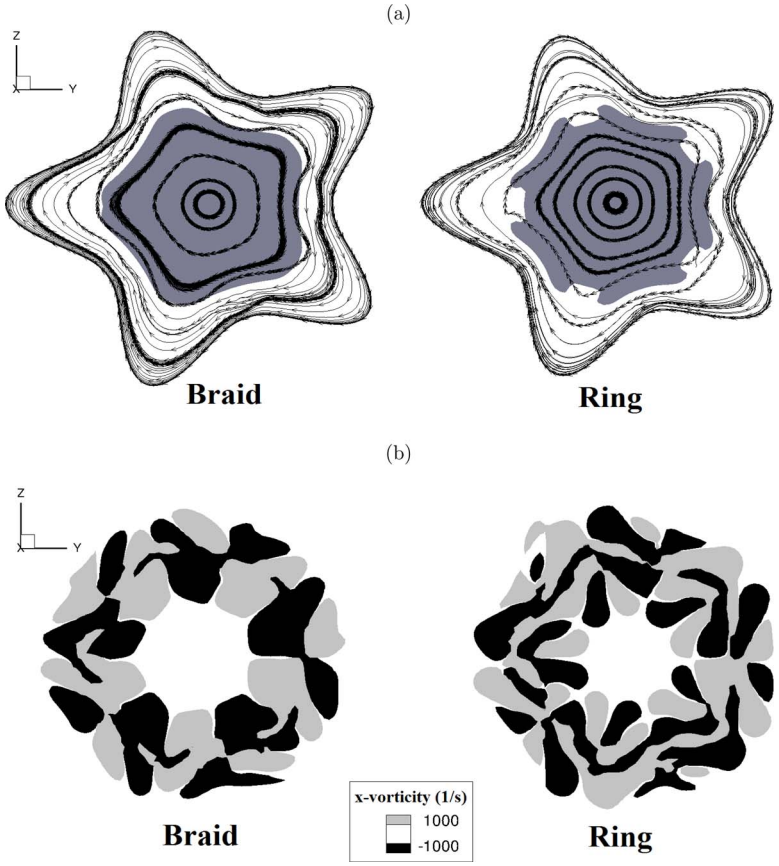

FIG. 34. (a) Jet cross-section in the braid and adjacent ring: lobes and projection of the vertex lines on the yz plane (b) azimuthal distribution of the streamwise vorticity: initial velocity perturbation $1 + 0.1\sin(5\theta)$ at t $= 10$ μs, $\frac{\rho_g}{\rho_l} = 0.1$, $Re = 1600$ and $We = 230\,000$.

perturbation mode number and five lobes have appeared. The projection of the vortex lines on this plane shows five hairpin vortices in the azimuthal direction. The vortex lines close to the center of the jet remain circular. Note that the location of the hairpin vortices coincides with the deformation of the liquid jet in the braid region. That is, the lobes are forming with a phase difference with respect to the hairpin vortices in the braid. This situation is similar to the non-perturbed initial conditions, i.e., natural mode ($m = 4$) as discussed in Fig. 30. The results for $m = 3$ not shown here demonstrate three hairpin vortices and three lobes in the yz plane at 10 μs. This confirms the fact that the number of the hairpin vortices, i.e., the mode number of the primary Widnall instability, is equal to the perturbation mode number.

Fig. 34(b) indicates the distribution of the streamwise vorticity for the same braid and ring shown in Fig. 34(a). As expected from the orientation of the hairpin vortices, five pairs of streamwise vorticity form in the azimuthal direction in the braid. Two sets of counter-rotating streamwise vorticity can be detected in the ring: first, the hairpin vortices in the ring itself and, second, the hairpin vortices from the upstream braid. The direction of the streamwise vorticity in the ring is opposite to that of the braid as was discussed for natural mode in Fig. 23. The conclusion is that weak forcing of azimuthal perturbation has little effect and the natural mode of lobes (four in the case studied here) will eventually develop. However, strong forcing can lead to a different number of lobes associated with forcing mode number. High resolution calculations (50% decrease in mesh size in all three directions) are consistent with our previous results in terms of the presence of four lobes in the azimuthal direction for non-perturbed flow and its orientation at 45° at lower Reynolds number, i.e., 1600. Thus, it is concluded that the numerical errors do not trigger an unreal mode number (m = 4) and do not force the present orientation of the lobes in the azimuthal direction for axisymmetric, i.e., non-perturbed initial conditions.

The vortical structures resulting from V-shape and A-shaped notched nozzles studied in the work of Cai, Tsai, and Liu[40] showed that the streamwise vortex pairs emerged only at peak and trough locations. Furthermore, the shape of the nozzle or the perturbation of the outer flow resulted in a deviation of the distribution of the counter-rotating vortex pairs with respect to that of the axisymmetric case.

D. Streamwise vorticity production

Investigation of the production of the streamwise vorticity is crucial to understand the origin of the three-dimensional instability for non-homogenous jets. Production of the streamwise vorticity as a result of vortex stretching and vortex tilting, i.e., strain-vorticity interactions and baroclinic effects are compared for a range of density ratios in Figs. 35–37 for the ring region. Equation (7) denotes the rate of change of streamwise vorticity in the cylindrical coordinate neglecting the effects of viscous diffusion:

$$\frac{D\omega_x}{Dt} = \omega_r \frac{\partial u}{\partial r} + \frac{\omega_\theta}{r}\frac{\partial u}{\partial \theta} + \omega_x \frac{\partial u}{\partial x} + \frac{1}{r\rho^2}\left[\frac{\partial \rho}{\partial r}\frac{\partial p}{\partial \theta} - \frac{\partial \rho}{\partial \theta}\frac{\partial p}{\partial r}\right], \tag{7}$$

where ω_x, ω_r, ω_θ, u, ρ, and p denote streamwise, radial, and azimuthal vorticity, streamwise velocity, density, and pressure, respectively. The terms on the right side are radial tilting, azimuthal tilting, and axial (streamwise) stretching, baroclinic effect due to azimuthal pressure gradient, and baroclinic effect due to radial pressure gradient, respectively. The component of pressure gradient that is tangential to the liquid-gas interface has been considered to account for the tangential body force acting on the liquid at that interface. The significance of the tangential component of the force acting on the liquid and its effect on production of vorticity and Rayleigh-Taylor instability were discussed in Secs. II A and II C. Density varies normal to the liquid interface, i.e., approximately in the radial direction. The gradients have been calculated along the computational interface thickness as described in Sec. III that equals to three mesh points in the radial and tangential directions. The gradient of the density in the azimuthal direction is negligible compared to its gradient in the radial direction since the jet cross-section remains circular for early stages of instability development. Therefore, we consider the radial density gradient and tangential component of pressure gradient in the baroclinic term. The absolute magnitude of each term on right-hand side of Eq. (7) has been calculated at

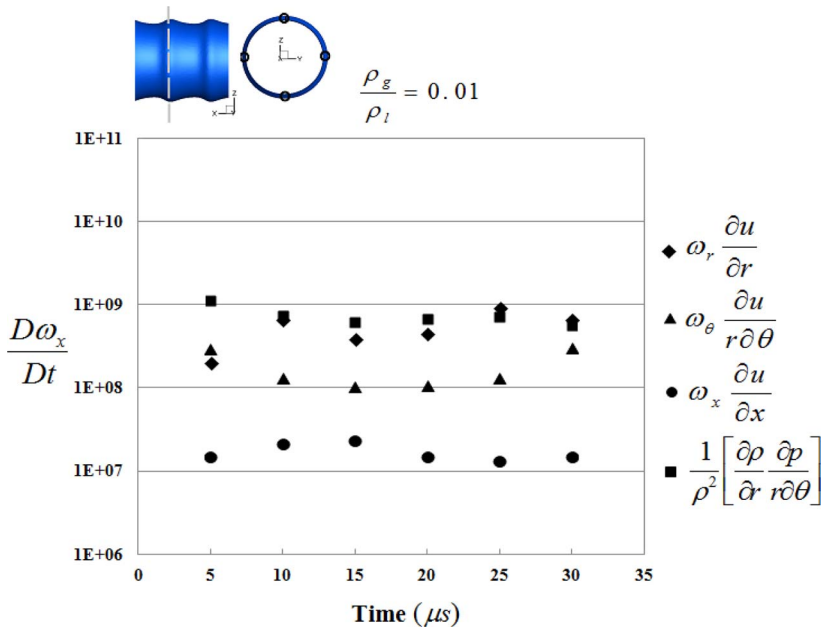

FIG. 35. Production rate of streamwise vorticity vs. time considering the effects of radial and azimuthal tilting, baroclinic effect, and streamwise stretching in the ring region for $\frac{\rho_g}{\rho_l} = 0.01$ ($Re = 1600$, $We = 230\,000$, $a = 800\,000$ m/s^2).

four different points around the liquid jet shown in Figs. 35–37. The average values of those points are reported here. The order of magnitude is important to us in comparing terms and the largest magnitudes appear near the surface. The local radial gradients will be affected by the size of the fuzzy interface thickness. However, in Subsection VI E, it will be shown that the circulation, which is an important integrated quantity, will not be affected.

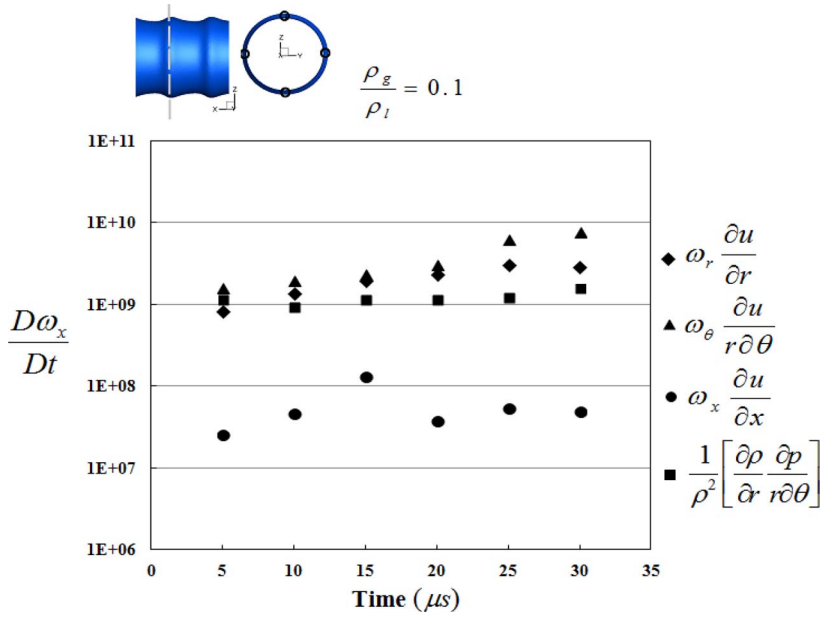

FIG. 36. Production rate of streamwise vorticity vs. time considering the effects of radial and azimuthal tilting, baroclinic effect, and streamwise stretching in the ring region for $\frac{\rho_g}{\rho_l} = 0.1$ ($Re = 1600$, $We = 230\,000$, $a = 800\,000$ m/s^2).

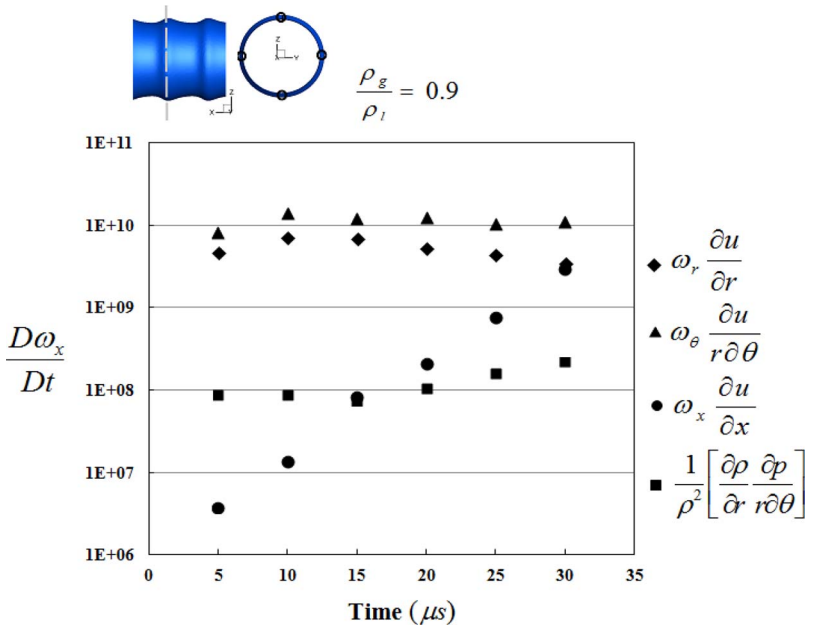

FIG. 37. Production rate of streamwise vorticity vs. time considering the effects of radial and azimuthal tilting, baroclinic effect, and streamwise stretching in the ring region for $\frac{\rho_g}{\rho_l} = 0.9$, ($Re = 1600$, $We = 230\,000$, $a = 800\,000$ m/s^2).

As Fig. 35 depicts, radial tilting and baroclinic effects are the dominating terms for density ratio equal to 0.01. The baroclinic term is slightly larger than the radial tilting term up to 20 μs in production of streamwise vorticity in the ring region. The radial tilting dominates the baroclinic effect later in time. Therefore, Rayleigh-Taylor instability is the primary cause of appearance of the transverse instability and deviation from axisymmetry at early times for low gas-to-liquid density ratios, i.e, low pressure surrounding gas. At a later time, the magnitude of the radial tilting becomes larger. The axial stretching effects are not very significant compared to radial and azimuthal tilting and baroclinic effect in this case as Fig. 35 shows.

Comparing Figs. 36 and 37 indicates that, for high gas-to-liquid density ratios, azimuthal tilting, radial tilting, and axial stretching increase significantly compared to that of Fig. 35. In Fig. 36, the baroclinic effect is larger than the radial stretching at 5 μs; however, radial stretching dominates the baroclinic effect at later times. Axial stretching and radial tilting increase with time for gas-to-liquid density ratio equal to 0.1. For gas-to-liquid density ratio equal to 0.9 shown in Fig. 37, the azimuthal tilting term is dominating the radial tilting and the baroclinic terms. The baroclinic term is smaller than that of lower density ratios since the density gradient in the radial direction is smaller for this case. The vortex stretching increases drastically for density ratio equal to 0.9 compared to previous cases. Therefore, for high pressure ambient air, i.e., higher density ratios, the baroclinic effect is not the major factor in the production of streamwise vorticity; however, azimuthal tilting plays an important role in the generation of the streamwise vorticity and deviation from axisymmetry. The baroclinic effect is an important factor at early stages for lower gas-to-liquid density ratios.

The average values of streamwise, azimuthal, and radial vorticity on the ring with respect to time has been plotted in Figs. 38, 39, and 40 for gas-to-liquid density ratios equal to 0.01, 0.1, and 0.9, respectively. As Fig. 38 demonstrates, the streamwise vorticity is larger for lower gas-to-liquid density ratios at early times. However, the streamwise vorticity increases drastically and remains higher for higher gas-to-liquid density ratios later in time, i.e., after 15 μs. As is shown in Fig. 35, the baroclinic effect dominates the azimuthal and radial stretching for gas-to-liquid density ratio equal to 0.01 up to 20 μs. Therefore, its streamwise vorticity is larger than that of the case with gas-to-liquid density ratio equal to 0.9 that has the smallest baroclinic term. Although the baroclinic effect is not dominating for density ratio equal to 0.1, its overall streamwise vorticity production is larger than that of the 0.01 and 0.9 cases at early times. (See Fig. 36.) The difference between gas-to-liquid

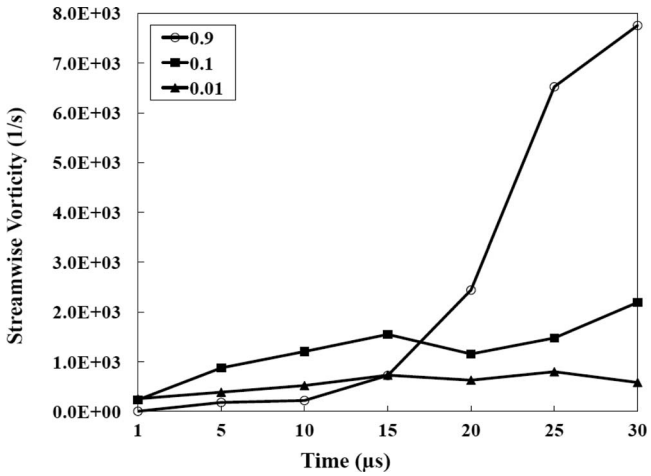

FIG. 38. Effects of gas-to-liquid density ratio on average value of streamwise vorticity vs. time ($Re = 1600$, $We = 230\,000$, $a = 800\,000$ m/s^2).

density ratio equal to 0.01 and 0.1 is negligible at 1 μs. As Fig. 37 shows, the azimuthal and radial tilting, and streamwise vortex stretching become noticeably larger for density ratio equal to 0.9 at later times. Therefore, the streamwise vorticity is smaller for this case at early times; however, it overtakes the values of streamwise vorticity in lower gas densities later in time.

Figs. 39 and 40 demonstrate that the average values of the azimuthal and radial vorticity are more significant and remain nearly constant for density ratio equal to 0.9. The smaller gas boundary layer for higher gas density produces larger velocity gradients near the interface that produces large values of azimuthal and radial vorticity compared to the cases with density ratios equal to 0.01 and 0.1. Therefore, vorticity tilting and stretching are larger for high density ratios as discussed earlier. A general conclusion is that the importance of the Rayleigh-Taylor baroclinic effect in promoting a three-dimensional instability has been overemphasized in the literature, especially for high pressure environments. Other important terms have not been carefully evaluated in the liquid-jet literature. The convergence of each source term in the vorticity equation with mesh refinement will be discussed in Sec. VI E.

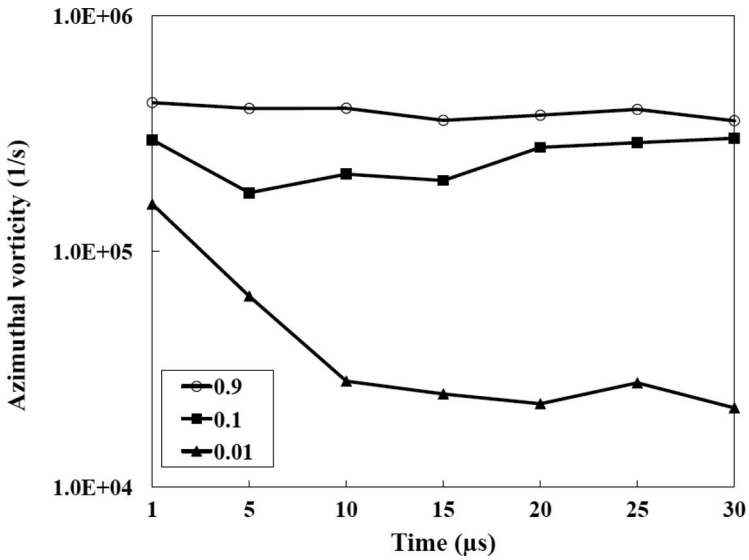

FIG. 39. Effects of gas-to-liquid density ratio on average value of azimuthal vorticity vs. time ($Re = 1600$, $We = 230\,000$, $a = 800\,000$ m/s^2).

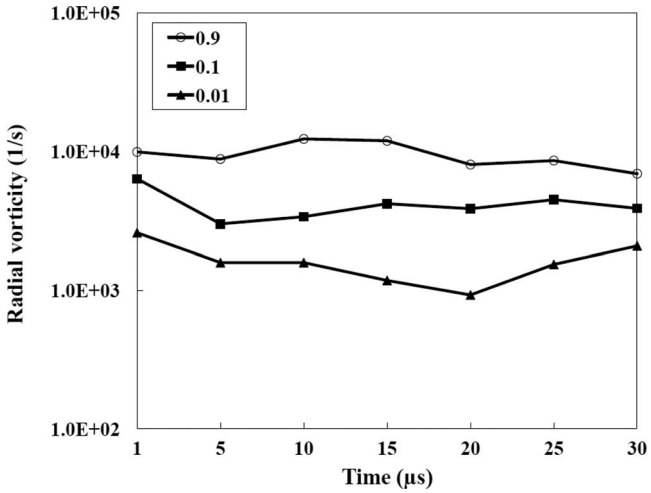

FIG. 40. Effects of gas-to-liquid density ratio on average value of radial vorticity vs. time ($Re = 1600$, $We = 230\,000$, $a = 800\,000$ m/s^2).

TABLE II. Different computational cases.

Case	Mesh size (μm)	Fuzzy interface thickness (μm)	Percent error (%) at 30 μs
1	5	15	+3.7
2	4	12	+2.5
3	5	30	− 25
4	2.5	15	+13.5
5	2.5	7.5	–

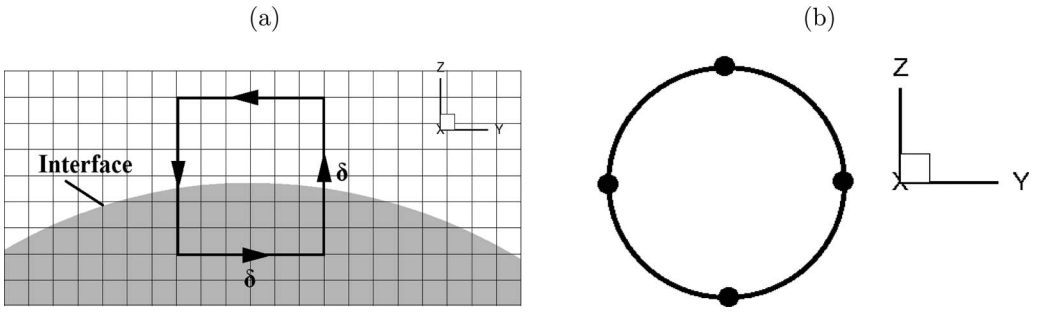

FIG. 41. (a) A schematic of the liquid-gas interface and the integration path in the yz plane. (b) Azimuthal location of the four integrating paths.

E. Error estimation

The interface thickness used in the level-set method is a pre-defined zone where the fluid properties, i.e., fluid density and viscosity vary smoothly in that thin region. Away from this zone, the liquid density and viscosity remain constant in each phase, i.e., liquid or gas. Five different cases have been considered here as Table II indicates. The velocity, pressure, and density gradients in Eq. (7) have been calculated based on Case 1, i.e., interface thickness equal to three-mesh-sizes where the mesh size is 5 μm. In those calculations, the order of magnitude of each term must be considered. A check that these orders of magnitude have been obtained accurately is accomplished by calculating the circulation on a given perimeter of a small rectangular region (30 μm × 30 μm) containing the fuzzy interface zone for the five different cases identified in Table II. A schematic of the liquid-gas

interface in the yz plane and the integration path is shown in Fig. 41. Since the rate of production of streamwise component of vorticity has been considered here, the circulation has been calculated in the yz plane. Four rectangular integration paths were examined in the yz transverse plane and the absolute magnitudes of circulation along those four paths were averaged to determine the error at 30 μs. These four paths were located at 90° intervals as is schematically shown in Fig. 41(b). Each of the four rectangular paths enclosed a portion of the surface crest where a counter-rotating vortex pair formed. The rate of change of streamwise vorticity and circulation can be related via Stoke's theorem as indicated in Eq. (8a). Considering the baroclinic term in Kelvin's circulation theorem as shown in Eq. (8b), the rate of production of the streamwise vorticity is proportional to the gradient of density in the transverse direction, i.e., z, and gradient of pressure in y direction. The pressure gradient in the y direction can be assumed constant compared to the density gradient in the fuzzy zone. Now, by combining Eqs. (8a) and (8b) and integrating along the constant length of the fuzzy zone, Eq. (8c) is obtained:

$$\frac{D\Gamma}{Dt} = \frac{D}{Dt}\iint_A \omega_x \, dy \, dz, \tag{8a}$$

$$\frac{D\Gamma}{Dt} \approx \int_A \frac{\nabla\rho \times \nabla p}{\rho^2} \, dy \, dz \approx \int_A \frac{1}{\rho^2}\left(\frac{\partial\rho}{\partial z}\frac{\partial p}{\partial y}\right) dy \, dz, \tag{8b}$$

$$\frac{D}{Dt}\int_\delta \omega_x \delta \, dz \approx \delta\frac{\partial p}{\partial y}\int_\delta \frac{1}{\rho^2}\frac{\partial\rho}{\partial z} \, dz \approx -\delta\frac{\partial p}{\partial y}\Delta\left(\frac{1}{\rho}\right), \tag{8c}$$

where Γ, A, and δ are the circulation, area and the length of the fuzzy zone in both y and z directions, respectively. Referring to Eq. (8c), the order of magnitude of the rate of change of circulation around a small rectangle in the fuzzy zone is approximately independent of the fuzzy-zone thickness.

Simulations with a refined mesh, i.e., 20% and 50% decrease in mesh size in all directions and in fuzzy interface thickness compared to Case 1 have been performed. Table II presents the average percent error referenced to Case 5 of the absolute magnitude of the circulation averaged around the same selection of rectangular paths at 30 μs after the start of simulations for Cases 1, 2, 3, and 4. These percent errors for Case 1 and Case 2 with respect to Case 5 with proportional changes in both mesh size and fuzzy zone thickness are equal to 3.7% and 2.5%, respectively. To explore the effects of fuzzy zone thickness irrespective of the mesh size, Cases 4 and 5 have been considered. The percent error of the average magnitude of the circulation around the same rectangular path at 30 μs after the start of simulations for Case 4, taking Case 5 as the reference, is equal to 13.5%. Finally, the percent error in the absolute value of circulation due to mesh refinement for Case 3 compared to Case 5, taking Case 5 as the reference is equal to 25%. This error is small for the relatively coarse mesh that we are considering. Still, the mesh and fuzzy zone thickness for Case 3 appear to be too crude. Cases 1 and 4 indicate that circulation magnitude decreases as mesh size decreases. Comparison of Cases 4 and 5 shows that circulation increases as the fuzzy zone thickness decreases. Proportional decrease in mesh size and fuzzy zone thickness shown in Cases 1, 2, and 5 causes a slight increase in circulation.

Fig. 42 shows the modification of the magnitudes of the four vorticity production terms for vortex tilting, vortex stretching, and baroclinic effect discussed in Sec. VI D under 50% refinement of both the mesh size and the fuzzy zone thickness. Results are shown for Case 1 (solid symbols) and Case 5 (open symbols) introduced in Table II for gas-to-liquid density ratio equal to 0.1 for 20, 25, and 30 μs. This figure demonstrates that the dominant effects in production of streamwise vorticity have been predicted by our method with sufficient accuracy to explain the physics.

One of the concerns in applying the level-set method for interface tracking is the conservation of mass. The re-initialization technique[61] and *ad hoc* mass conservation method used in this work calculates the liquid mass at each time step and compensates the mass loss by a small factor. This improves the mass conservation of the level-set method. We expect constant liquid volume in the liquid-segment model during the injection period as the periodic velocity boundary conditions on the right and left boundaries of the computational domain in Fig. 11 implies. However, there are two

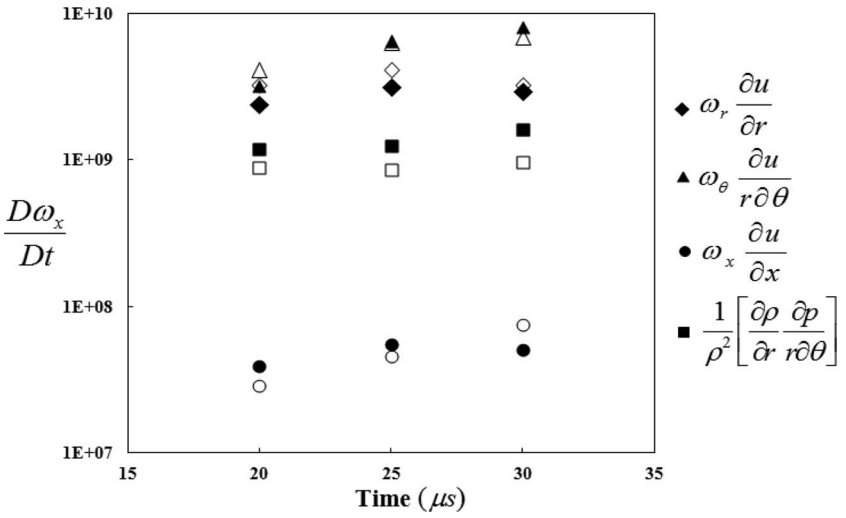

FIG. 42. Convergence of source terms in the vorticity equation with mesh refinement. Case 1: solid symbols, Case 5: open symbols, $\frac{\rho_g}{\rho_l} = 0.1$ ($Re = 1600$, $We = 230\,000$, $a = 800\,000$ m/s^2).

factors affecting the liquid volume: first, the level-set method deficiency in mass conservation, and, second, the detachment of the liquid particles from the liquid jet when the size of the liquid protrusions becomes comparable to the grid size. The percent error in liquid mass for Case 1 and Case 3 remain below 0.3% and 0.25%, respectively, during the first 100 μs after the start of simulations. In fact, the percent error is below 0.001% for the first 50 μs after the start of simulations for both cases since liquid detachment has not occurred significantly at that time.

F. Vorticity structures in ligaments

In this section, the vorticity structure inside a ligament is studied. The goal is to investigate whether the liquid ligaments that form from the elongation of the lobes show qualitatively the same vorticity structure as single-phase flows; i.e., they expel from the jet core similar to the side-jets as counter-rotating vortex pairs (see Fig. 5). Fig. 43(a) shows a cross section of the jet in the xy plane at 84 μs including liquid ligaments. In this figure, three ligaments have been shown. None of these ligaments are detached from the core; however, since none of these three ligaments are in the same plane only one of them appears almost completely on this plane. Fig. 43(b) indicates the pressure variation along two of the slender ligaments shown in Fig. 43(a). The pressure increases from the root of the ligament toward its tip and the center of the ligament has the highest pressure. If we examine another ligament later in time, the ligament becomes thinner locally as Fig. 44(a)

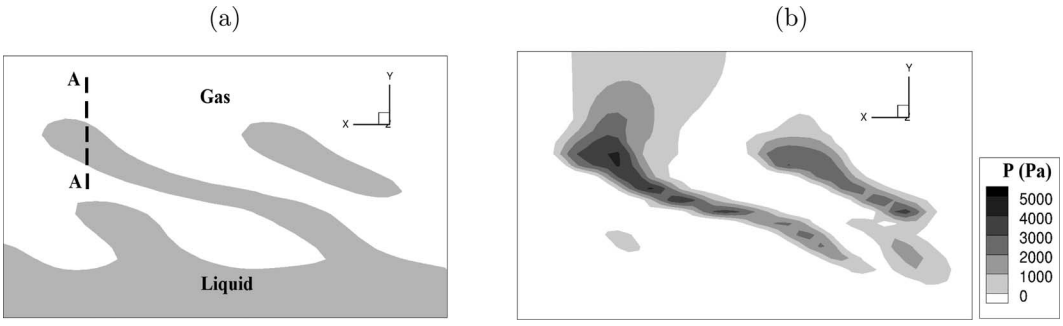

FIG. 43. (a) Liquid-gas interface in the xy plane showing ligaments (b) pressure contour, at $t = 84$ μs, $\frac{\rho_g}{\rho_l} = 0.1$, $Re = 1600$, $We = 230\,000$, $a = 800\,000$ m/s^2 (gas flows from right to left).

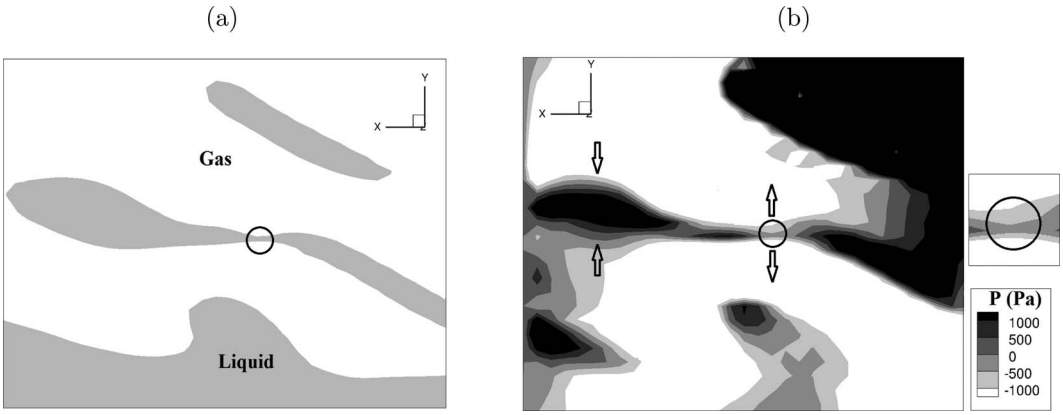

FIG. 44. (a) Liquid-gas interface in the *xy* plane showing a ligament with varying cross-sectional area (b) pressure contour, at $t = 89\ \mu s$, $\frac{\rho_g}{\rho_l} = 0.1$, $Re = 1600$, $We = 230\,000$, $a = 800\,000\ \text{m/s}^2$ (gas flows from right to left).

depicts. The pressure contours on the same ligament shown in Fig. 44(b) indicate the change in the direction of the pressure gradient along the ligament. The absolute value of the pressure decreases toward the center of the ligament at the smallest cross-sectional area (see the magnified picture); however, the pressure decreases radially outward at the tip of the ligament. The arrows depict the change in the direction of the pressure gradient. Therefore, there is an oscillation of the pressure gradient inside a ligament that produces a waviness on its surface.

Fig. 45(a) shows the pressure contour in slice AA indicated by the dashed line in Fig. 43(a). The location of the ligament in this perspective is demonstrated with a solid circle. Fig. 45(b) shows the streamwise vorticity contours in the ligament in cross-section AA. It can be seen that the streamwise vorticity changes sign inside the ligament. Therefore, counter-rotating vortex structures exist both near the lobes in the gas phase as was shown in Fig. 31 and inside the elongated ligament. This vorticity structure was found in every other liquid ligament around the jet at different times that was examined in detail here. For example, Fig. 46 indicates the projected vortex lines on a liquid ligament at 60 μs. The vortex lines turn in the ligament producing hairpin vortices, i.e., counter-rotating vortex pairs in the streamwise direction. The arrows demonstrate the direction of the vorticity projected on the ligament. The sink point shown near the tip of the ligament is actually the projection of the vorticity component normal to the surface of the ligament.

In conclusion, the side-jet phenomena in homogenous jets is similar to the formation of the ligaments in two-phase jet flow based on the vortical structures. However, for non-homogenous jet flow, capillary force plays a significant role in defining the shape of the ligaments and their break-up

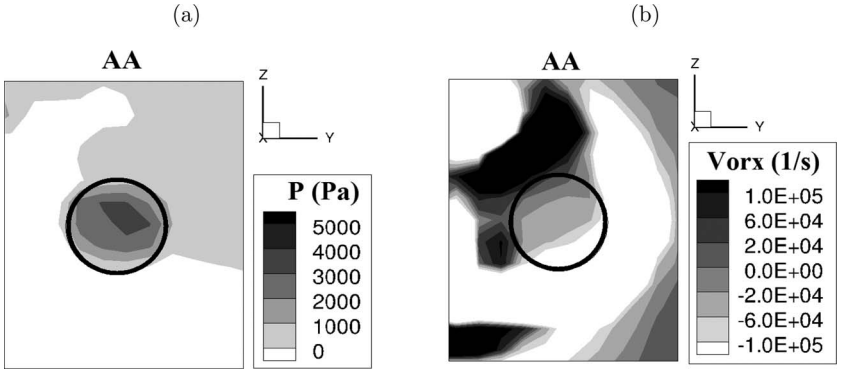

FIG. 45. (a) Cross-section AA showing the ligament in the *yz* plane (solid circle) (a) pressure contour, (b) streamwise vorticity contour at $t = 84\ \mu$s, $\frac{\rho_g}{\rho_l} = 0.1$, $Re = 1600$, $We = 230\,000$, $a = 800\,000\ \text{m/s}^2$.

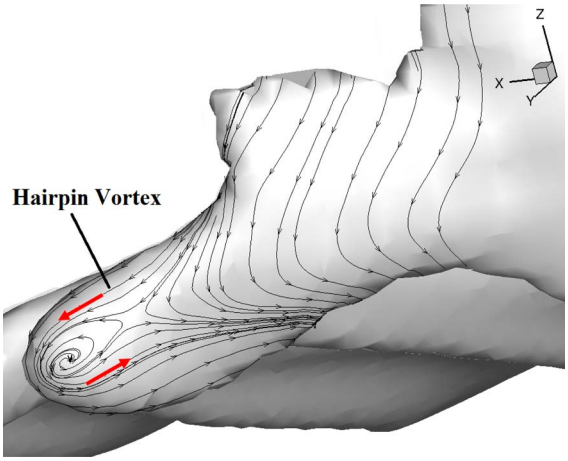

FIG. 46. Projected vortex lines on a ligament showing hairpin vortices at t = 60 μs, $\frac{\rho_g}{\rho_l} = 0.1$, $Re = 1600$, $We = 230\,000$, $a = 800\,000$ m/s^2.

from the jet core into the droplets. It is commonly stated in the literature that capillary forces are dominant and act at a very short time scale to fragment the elongated ligament into droplets.[1,2] According to Shinjo and Umemura,[2] capillary waves in the short-wave mode propagate inside the ligament and decrease the surface area of the ligament locally. Surface tension pinches the ligament at minimum cross-sectional area. However, the large streamwise vorticity observed inside the ligament might produce a large angular momentum and compete with the capillary force.

To investigate whether this inertia force dominates the capillary force, a new Weber number is defined. The radial pressure gradient due to the transverse velocity difference is $\frac{dp}{dr} \sim \frac{\rho_l(\Delta v)^2}{R}$, where $\Delta v = O(R\omega_x)$ is the transverse velocity deference as a result of the streamwise vorticity inside the ligament with the average radius R. The radial pressure gradient due to surface tension is $\frac{dp}{dr} \sim \frac{\sigma}{R}$. The ratio of these two pressure gradients is the resultant We, i.e., $We = \frac{\rho_l R(\Delta v)^2}{\sigma} = \frac{\rho_l \omega_x^2 R^3}{\sigma}$. Note that these two pressure gradients have different signs. If this We is much larger than one, the vorticity effects inside the ligament can be more important than the capillary force. For the ligament shown in Fig. 45 where its liquid density, surface tension coefficient, ligament radius, and maximum value of streamwise vorticity are 804 kg/m^3, 0.028 N/m, 15 μm, and 10^5 1/s, respectively, the defined We is 0.97. For other ligaments investigated here the We is close to one. Therefore, inertia force can at least be important even if capillary forces dominate the ligament break-up. The resultant force likely produces the waviness seen on the ligaments in experiments and numerical simulations.

As the ligament elongates and its cross-sectional area decreases, the vorticity does not increase substantially along the ligament due to strong viscous forces acting on the ligament. A Re based on the liquid viscosity and density, ligament radius, and velocity due to the streamwise vorticity, i.e., $v = R\omega_x$ defined as $Re = \frac{\rho_l \omega_x R^2}{\mu_l}$ varies between 1 and 10 and the We is less than one for all the elongated ligaments examined here. Therefore, capillary forces will dominate the pressure gradients due to the angular momentum and pinching off occurs for longer ligaments at the smallest cross-sectional areas. A detailed study of the vorticity dynamics inside the ligaments requires high resolution computations that will be performed in the near future.

VII. CONCLUSION AND SUMMARY

The Navier-Stokes equations and level-set method were used to simulate the behavior of a liquid jet injected into high pressure air during the start-up period of injection. The axisymmetric model of full liquid jet instability predicted unstable wavelengths consistent with linear instability theories and experiments. Then, a less computationally intensive case was studied with a segment of the jet core undergoing axisymmetric temporal instability; agreement with the full-jet calculation is satisfactory justifying the segment analysis for three-dimensional computations. The axisymmetric

results showed that, the higher the relative velocity and/or the lower the surface tension, the shorter are the values of the most unstable wavelengths. The effects of acceleration are more significant at early times of injection. Very small-scale instabilities form at the jet interface for high injection accelerations. The axisymmetric calculations produce secondary instabilities which build on the original KH instability. However, those take longer to manifest than three-dimensional secondary instabilities. Consequently, they have no presence in the three-dimensional computations.

The results of the three-dimensional computations for liquid-segment agree at very early times with the axisymmetric results. Three-dimensional instability starts as a result of the appearance of counter-rotating pairs of streamwise vorticity in the braid region, i.e., between two consecutive vortex rings similar to three-dimensional mixing layers. These vortical structures are actually hairpin vortices that wrap around the vortex rings, i.e., crests of KH waves and produce a number of lobes by distortion and deformation of vortex rings. These lobes elongate later in time and produce the ligaments consistent with experimental observations. The dynamic mechanisms for the formation of lobes and ligaments and the creation of streamwise vorticity are shown to be identical. The development of hairpin vortices is the essential dynamic feature that unifies the phenomena. The sign of the pairs of streamwise vorticity in the ring is reversed compared to that of the braid since the vortical structures originate from the braid first and wrap around the neighboring ring. This situation has been seen in like-density jets. The hairpin vortices on the crests appear at a 45° position with respect to the hairpin vortices in the braid consistent with homogenous results.

A natural mode number of lobes exists for a given configuration and cannot be changed by weak forcing; however, strong forcing can produce a different number of lobes associated with the mode number of the velocity perturbations. For the Reynolds number and Weber number studied, four lobes was the natural selection. The number of hairpin vortices, i.e., counter-rotating vortex pairs is equal to the azimuthal mode of perturbation.

A hole can be formed at the surface of the lobe as a result of the stretching of the lobe and the surface tension force. When the hole expands it tears and two ligaments form from each lobe. For low gas-to-liquid density ratios, ligaments mostly form due to elongation of the lobes itself; however, most of the ligaments form as a result of hole tearing for higher density ratios. As surface tension is reduced, i.e., We increases, the deviation from axisymmetry starts earlier in time and maintains a larger magnitude. As liquid viscosity decreases (increased Re), deviation from axisymmetry becomes slower but more lobes appear.

Azimuthal instabilities appear on the liquid jet as a result of production of pairs of streamwise vorticity for both low and high gas-to-liquid density ratios. The baroclinic effect due to the radial component of density gradient and the tangential component of pressure gradient is the dominant mechanism in production of streamwise vorticity for lower gas-to-liquid density ratios at early times. However, azimuthal and radial vortex tilting will overcome the baroclinic effect later. Azimuthal tilting dominates the baroclinic, radial tilting, and axial stretching for higher gas-to-liquid density ratios. At very high gas-to-liquid density ratios, the magnitude of streamwise vorticity is smaller than that of lower gas-to-liquid density ratios at early times since the baroclinic effect is negligible. However, azimuthal and radial tilting and axial stretching surpass those of lower gas-to-liquid density ratios later in time. Therefore, the formation of the lobes, i.e., streamwise vortical structures appear later in time for higher gas-to-liquid density ratios with respect to a dimensional time. The azimuthal and radial components of vorticity are larger for higher density ratios. The conclusions about the order of magnitudes of the streamwise vorticity generation rates did not depend on the selected numerical thickness of the interface for the level-set calculations and mesh size. Generally, the importance of baroclinic vorticity production has been overemphasized in the literature, especially at very high pressures. Other important aspects of vorticity dynamics and similarities with liquid injection into like-fluid have also been neglected.

Counter-rotating streamwise vorticity was observed inside the ligaments revealing the similarities between the ligament formation in two-phase flows with side-jet phenomenon in like-density jets. These counter-rotating vortices were actually hairpin vortices developed in the ring region that formed the lobes at early times. The inertia force due to high streamwise vorticity inside the ligaments opposes the capillary forces acting on the ligaments. The interaction of these two forces likely explains the waviness on the elongated ligaments observed in experiments.

ACKNOWLEDGMENTS

The authors gratefully acknowledge support from The U.S. Army Research Office through Grant No. W911NF-09-1-0208 with Dr. Ralph A. Anthenien, Jr. as the Program Manager of Propulsion and Energetics. We would also like to acknowledge the valuable contribution of Dr. S. Dabiri at the Purdue University in developing the axisymmetric CFD code with level-set method used in this work. Dr. P. Popov at UCI is thanked for his significant role in obtaining high-resolution 3D results. Access to the NICS Kraken supercomputer was very valuable in performing our high resolution computations. Informative discussions with Professor E. Villermaux and Professor F. Hussain are greatly appreciated.

APPENDIX A: AXISYMMETRIC FULL JET

The independency of the solution on the size of the computational domain has been investigated. The difference in axial velocity of liquid points located on the axis of symmetry close to the jet tip (e.g., 2D downstream of the orifice at 20 μs after the start of injection) for a computational domain twice the length and height is less than 0.003%. The percent error of the penetration length is less than 2%. In addition, the unstable structures at the interface for these two computational domains show similarities in terms of wavelengths and shape of the sheets and the discrepancies between the thickness of the protrusions at the back of the jet cap is less than 0.005%. The liquid-segment model will be used to evaluate the reliability of our level-set technique in terms of mass conservation.

Fig. 47 demonstrates the effects of grid-spacing on the size of the detached sheets from the interface for mesh sizes equal to half a micrometer (Case 1) and 1 μm (Case 2) in both axial and radial directions at 50 μs after the start of injection. These images show that a coarse grid produces thicker sheets and larger detached rings from the jet core. The sizes of the detached sheets are approximately equal to the grid-spacing in all three cases. Other than the size of detached sheets, two cases show similar behavior in terms of the jet axial velocity (1% error) and jet penetration lengths, i.e., the location of the furthest liquid point on the axis of symmetry (less than 2% error).

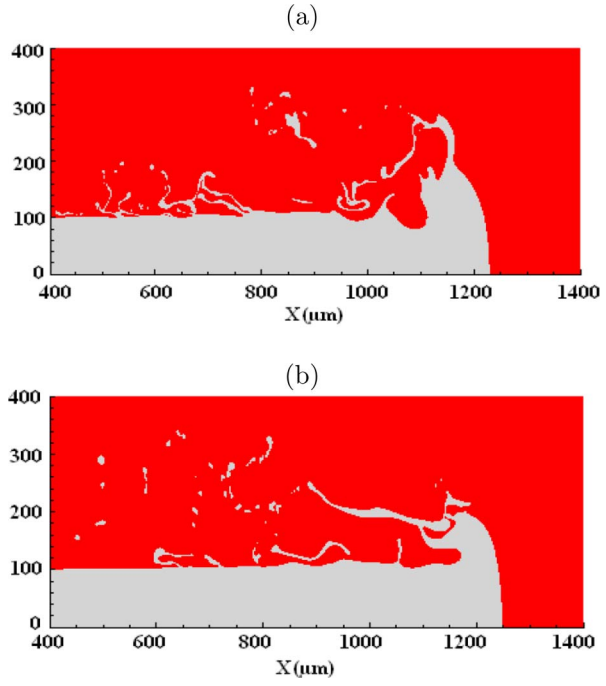

FIG. 47. Impact of grid-resolution at 50 μs, $\frac{\rho_g}{\rho_l} = 0.048$, $\Delta p_{max} = 1.6$ MPa, $Re = 16\,000$, $We = 230\,000$: (a) $\Delta x = \Delta r = 0.5$ μm, (b) $\Delta x = \Delta r = 1$ μm.

Comparing the wavelengths of similar protrusions observed for the three cases with different grid sizes at 50 μs shows that the coarser grid predict slightly larger wavelengths compared to Case 1, especially for smaller wavelengths. The appearance of small waves on the sheets indicates that surface tension is dominating for the small-scale protrusions and the grid-spacing is sufficient to capture the flow physics. However, the discrepancies are within a few micrometers that is not significant for wavelength prediction. Other discrepancies on that scale of few micrometers, such as the shape of the thin sheets and the size of the detached liquid particles, are inevitable in numerical simulations. In addition, the size of the rings that eventually detach from the liquid jet is scaled with

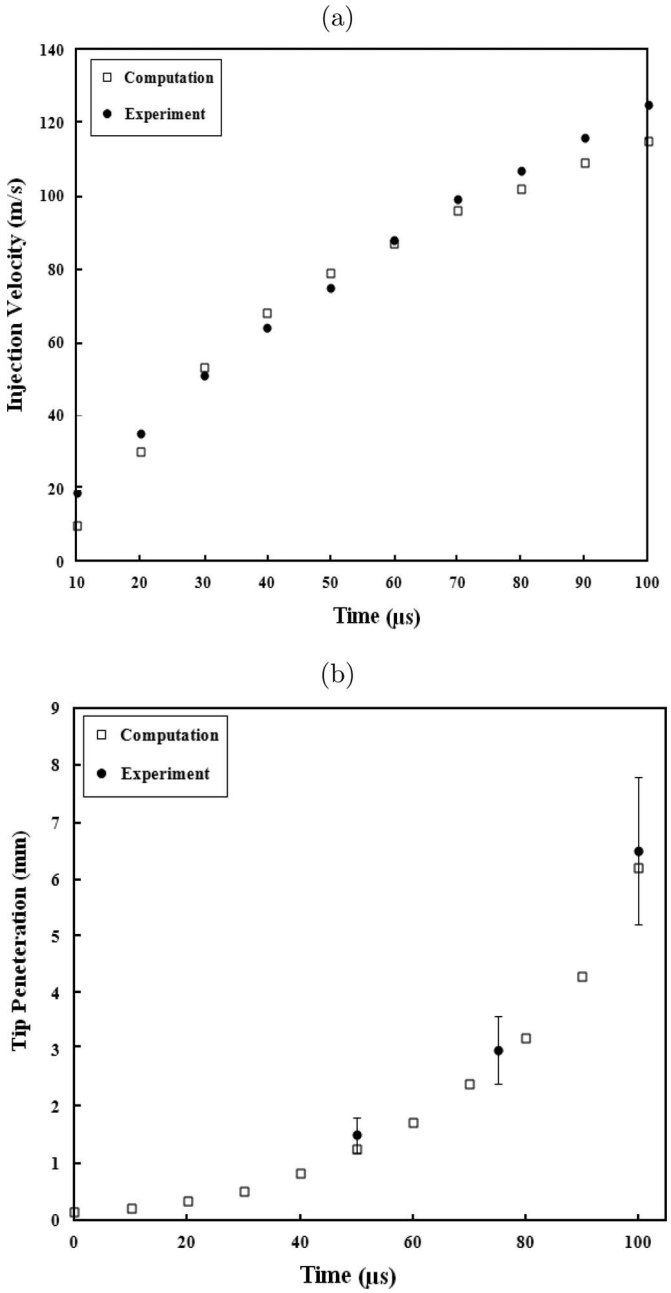

FIG. 48. (a) Spray injection velocity estimation by Turner *et al.*[23] and the present numerical model (b) jet tip penetration length for the first 100 μs of the injection for experiment of a seven-hole injector with Diesel fuel at 410 K injected into stagnant air at 20 MPa pressure. The error bars indicate 20% error in experimental data.

the secondary wavelengths on the sheets before they artificially break-off due to the deficiencies of the numerical method. Therefore, this error does not affect our simulation to a substantial extent.

In order to validate the numerical model of the present work, the experimental results of spray penetration lengths by Karimi[62] have been considered. In this experiment, the Diesel fuel at 410 K is injected through a seven-hole injector into stagnant air at 20 MPa with an injection pressure of 60 MPa. To avoid the complexities of the flow injector configuration and probable disturbances initiating from the nozzle and its consistency with the numerical model of the present work, use has been made of the approximate injection velocity profile based on the same experiment provided by Turner *et al.*[23] That profile is calculated from mass flow rate estimation for one of the seven holes of injector assuming the injection velocity is approximately constant in the axial direction. The above mentioned injection velocity profile has been produced by modifying the boundary conditions in the nozzle of the present numerical model for a one-by-one micrometer grid-spacing in both axial and radial directions.

Fig. 48(a) depicts the velocity profile suggested by Turner *et al.*[23] compared with that of the present work for the first 100 μs after the start of injection and Fig. 48(b) demonstrates the experimental and computed penetration lengths for the injection velocity shown in Fig. 48(a). We chose the first 100 μs of injection period since the early stages of start-up period have a great effect on primary atomization and overall break-up length of the jet. Although there were only three points available in the experimental data for this comparison during the first 100 μs of injection, the numerical model agrees well with the experiment in certain global features.

APPENDIX B: AXISYMMETRIC LIQUID-SEGMENT MODEL

Fig. 49 shows the range of KH and secondary wavelengths at the liquid/gas interface for the liquid-segment for 10–80 μs after the start of simulations for the liquid-segment of length 1 mm with *Re* and *We* equal to 16 000 and 230 000, respectively. Initially, KH waves in the range of 60–120 μm appear at the interface. Then, the wavelength range extends due to secondary instability resulting from the acceleration of the gas blowing over the crests of these waves. The smallest wavelengths on the spectrum designate the secondary wavelengths and the longer wavelengths indicate the KH instability. We detect waves as small as 10 μm in the spectrum, consistent with the full-jet simulation shown in Fig. 9(b).

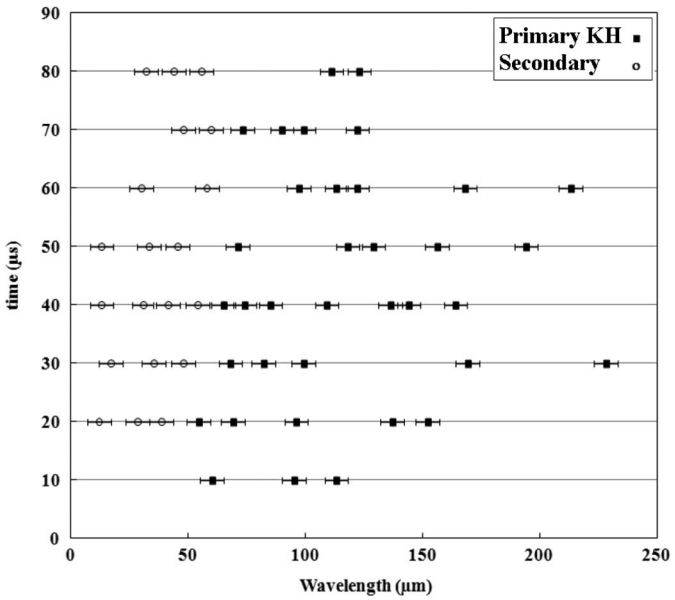

FIG. 49. KH and secondary wavelength spectrum during start-up vs. time for the liquid-segment numerical simulation, the error bars correspond to 5 μm ($Re = 16\,000$, $We = 230\,000$, $a = 800\,000$ m/s^2).

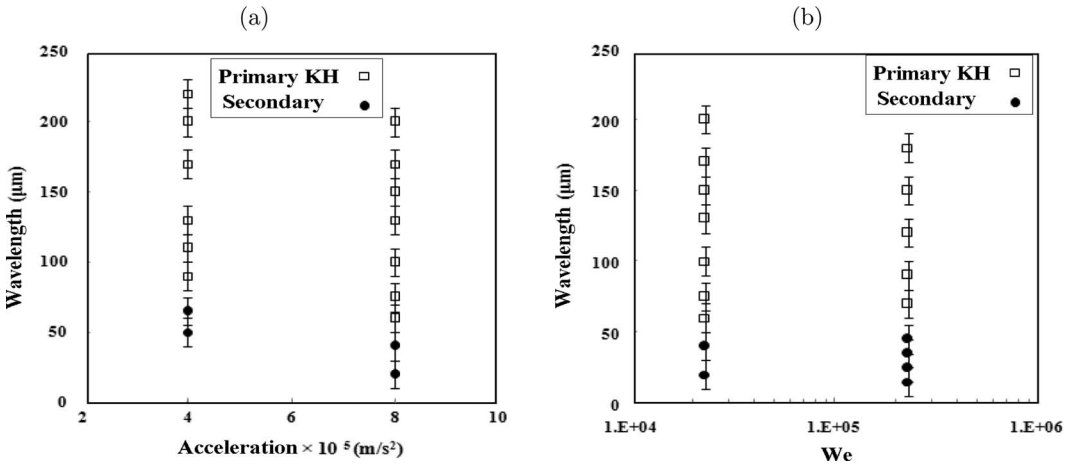

FIG. 50. Length of surface waves in axial and normal direction, i.e., KH and secondary wavelengths $t = 30$ μs, $Re = 16\,000$, $\frac{\rho_g}{\rho_l} = 0.048$, $\Delta p_{max} = 1.6$ MPa. (a) $We = 230\,000$ (b) $a = 800\,000$ m/s^2, error bars indicate 10 μm.

Note that full transient jet and liquid-segment cannot be exactly matched at a specific computational time due to the different nature of the analysis, i.e., spatial instability for full jet vs. temporal instability for liquid-segment model. However, the liquid-segment qualitatively agrees with the full jet and predicts the same range of wavelengths observed in full jet simulations. For example, the primary KH waves become longer and the secondary waves associated with them also increase in length as time elapses. This trend continues until the largest KH wave approach 250 μm and secondary waves grow to about 35 μm. The secondary instability must be studied together with KH instability which in turn is strongly dependent on the viscosity, density ratios, and the inertia of the two phases. As mentioned earlier, the liquid-segment model is useful for the time that the instabilities appear and KH waves form at the interface away from the mushroom-shaped cap at the interface.

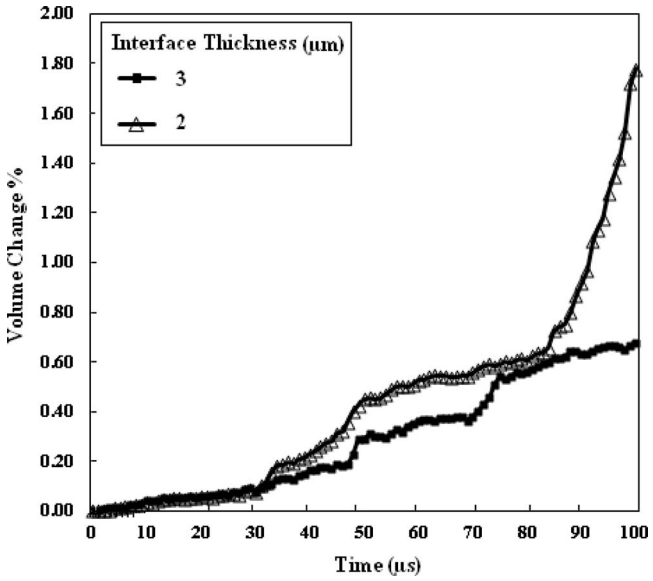

FIG. 51. Effects of interface thickness used in level-set method on liquid volume change with respect to the initial state in the liquid-segment during start-up, $Re = 16\,000$, $We = 23\,000$, $\frac{\rho_g}{\rho_l} = 0.048$, $\Delta p_{max} = 1.6$ MPa, $a = 800\,000$ m/s^2.

Fig. 50(a) compares the range of KH and secondary wavelengths with respect to the acceleration of the frame of reference for the same instants of time. Both types of waves are shorter for higher acceleration; however, the effects of acceleration on secondary wavelengths is more noticeable. Essentially, a Froude number based on wavelength is identical in these two cases. Fig. 50(b) demonstrates the effects of surface tension on interfacial wavelengths. Lower surface tension decreases the lengths of both KH and secondary wavelengths at comparable instants of time.

The liquid volume change with respect to the initial state during start-up changes from 0% to 0.7% after 100 μs after the start of computations for a 3 μm interface thickness keeping mesh spacing constant (1 μm). The sudden jumps in the graph corresponds to the local tearing of the liquid at the edge of the liquid cones which in turn depends on the computational grid size. Decreasing the level-set interface thickness leads to a sharper change in fluid properties between the two-phases and locally thinner ligaments that detach easier from the liquid jet compared with a 3 μm interface thickness. Therefore, the liquid volume change is higher for smaller interface thickness as Fig. 51 demonstrates. Interface thickness equal to 3 μm leads to acceptable mass conservation for the present simulations.

[1] P. Marmottant and E. Villermaux, "On spray formation," J. Fluid Mech. **498**, 73 (2004).
[2] J. Shinjo and A. Umemura, "Simulation of liquid jet primary break-up: Dynamics of ligament and drolpet formation," Int. J. Multiphase Flow **36**, 513 (2010).
[3] M. Herrmann, "On simulating primary atomization using the refined level set grid method," J. Atomiz. Sprays **21**, 283 (2011).
[4] J. Y. Koo and J. K. Martin, "Droplet sizes and velocities in a transient Diesel fuel spray," SAE Technical Paper No. 900397, 1990.
[5] G. J. Smallwood, O. L. Gulder, and D. R. Snelling, "The structure of the dense core region in a transient Diesel spray," Symp. (Int.) Combust. **25**, 371 (1994).
[6] O. L. Gulder, "Views on the structure of transient Diesel sprays," J. Atomiz. Sprays **10**, 355 (2000).
[7] W. Cai, C. F. Powell, Y. Yue, S. Narayanan, J. Wang, M. W. Tate, M. J. Renzi, A. Ercan, E. Fontes, and S. M. Gruner, "Quantitative analysis of highly transient fuel sprays by time-resolved X-radiography," Appl. Phys. Lett. **83**, 1671 (2003).
[8] W. Ning, R. Reitz, R. Diwakar, and A. Lippert, "A numerical investigation of nozzle geometry and injection condition effects on Diesel fuel injector flow physics," SAE Technical Paper No. 2008-01-0936, 2008.
[9] D. J. Kim and J. K. Lee, "Analysis of the transient atomization characteristics of Diesel spray using time-resolved PDPA data," Int. J. Auto. Tech. **9**, 297 (2008).
[10] A. I. Ramirez, S. Som, S. K. Aggarwal, A. L. Kastengren, E. M. El-Hannouny, D. E. Longman, and C. F. Powell, "Quantitative X-ray measurements of high-pressure fuel sprays from a production heavy duty Diesel injector," Exp. Fluids **47**, 119 (2009).
[11] L. M. Pickett, S. Kook, and T. C. Williams, "Transient liquid penetration of early injection Diesel sprays," SAE Int. J. Engines **2**, 785 (2009).
[12] A. L. Kastengren, C. F. Powell, T. Riedel, S. K. Cheong, K. S. Im, X. Liu, Y. J. Wang, and J. Wang, "Nozzle geometry and injection duration effects on Diesel sprays measured by X-ray radiography," Trans. ASME J. Fluid Eng. **130**, 1–12 (2008).
[13] R. Aneja and J. Abraham, "How far does the liquid penetrate in a Diesel engine: Computed results vs. measurements," Combust. Sci. Technol. **138**, 233 (1998).
[14] M. Linne, M. Paciaroni, T. Hall, and T. Parker, "Ballistic imaging of the near field in a Diesel spray," Exp. Fluids **40**, 836 (2006).
[15] C. M. Varga, J. C. Lasheras, and E. J. Hopfinger, "Initial break-up of a small-diameter liquid jet by a high-speed gas stream," J. Fluid Mech. **497**, 405 (2003).
[16] D. D. Joseph, J. Belanger, and G. S. Beavers, "Break-up of a liquid drop suddenly exposed to a high-speed air stream," Int. J. Multiphase Flow **25**, 1263 (1999).
[17] G. I. Taylor, "The instability of liquid surfaces when accelerated in a direction perpendicular to their planes," Proc. R. Soc. London, Ser. A **201**, 192 (1950).
[18] J. W. L. R. Strutt, "Investigation of the character of the equilibrium of an incompressible heavy fluid of variable density," Proc. London Math. Soc. **14**, 170 (1883).
[19] Lord Rayleigh, "On the stability, or instability of certain fluid motion," Proc. London Math. Soc. **11**, 57 (1880).
[20] M. R. Turner, J. J. Healey, S. S. Sazhin, and R. Piazzesi, "Wave packet analysis and break-up length calculations for accelerating planar liquid jets," Fluid Dyn. Res. **44**, 015503 (2012).
[21] S. Chandrasekhar, *Hydrodynamic and Hydromagnetic Stability* (Dover, 1961).
[22] N. Abani and R. D. Reitz, "Unsteady turbulent round jets and vortex motion," Phys. Fluids **19**, 125102 (2007).
[23] M. R. Turner, S. S. Sazhin, J. J. Healey, C. Crua, and S. B. Martynov, "A break-up model for transient Diesel fuel sprays," Fuel **97**, 288 (2012).
[24] M. Herrmann, "A balanced force refined level set grid method for two-phase flows on unstructured flow solver grids," J. Comput. Phys. **227**, 2674 (2008).
[25] M. Gorokhovski and M. Herrmann, "Modeling primary atomization," Ann. Rev. Fluid Mech. **40**, 343 (2008).
[26] H. Pitsch and O. Desjardins, "Detailed numerical investigation of turbulent atomization of liquid jets," J. Atomiz. Sprays **20**, 311 (2010).

[27] T. Funada and D. D. Joseph, "Viscous potential flow analysis of Kelvin-Helmholtz instability in a channel," J. Fluid Mech. **445**, 263 (2001).
[28] D. D. Joseph, T. Funada, and J. Wang, *Potential Flows of Viscous and Viscoelastic Liquids* (Cambridge University Press, 2008).
[29] D. D. Joseph, A. Huang, and G. V. Candler, "Vaporization of a liquid drop suddenly exposed to a high-speed air stream," J. Fluid Mech. **318**, 223 (1996).
[30] S. S. Hwang, Z. Liu, and R. D. Reitz, "Break-up mechanisms and drag coefficients of high-speed vaporizing liquid drops," J. Atomiz. Sprays **6**, 353 (1996).
[31] L. M. Ricart, R. D. Reitz, and J. E. Dec, "Comparisons of Diesel spray liquid penetration and vapor fuel distributions with in-cylinder optical measurements," J. Eng. Gas Turbines Power **122**, 588 (2000).
[32] E. Villermaux and C. Clanet, "Life of a flapping liquid sheet," J. Fluid Mech. **462**, 341 (2002).
[33] R. H. Rangel and W. A. Sirignano, "Nonlinear growth of Kelvin-Helmholtz instability: Effect of surface tension and density ratio," Phys. Fluids **31**, 1845 (1988).
[34] R. H. Rangel and W. A. Sirignano, "The linear and nonlinear shear instability of a fluid sheet," Phys. Fluids A **3**, 2392 (1991).
[35] J. W. Rottman and D. B. Olfe, "Comment on "Discretized simulation of vortex sheet evolution with buoyancy and surface tension effects," AIAA J. **15**, 1214 (1977).
[36] R. G. Zalosh, "Discretized simulation of vortex sheet evolution with buoyancy and surface tension effects," AIAA J. **14**, 1517 (1976).
[37] G. Tryggvason, "Numerical simulation of the Rayleigh-Taylor instability," J. Comput. Phys. **75**, 253 (1988).
[38] D. Liepmann and M. Gharib, "The role of streamwise vorticity in the near-field entrainment of round jets," J. Fluid Mech. **245**, 643 (1992).
[39] L. P. Bernal and A. Roshko, "Streamwise vortex structure in plane mixing layers," J. Fluid Mech. **170**, 499 (1986).
[40] C. Cai, H. M. Tsai, and F. Liu, "Numerical simulation of vortical flows in the near field of jets from notched circular nozzles," Comput. Fluids **39**, 539 (2010).
[41] J. E. Martin and E. Meiburg, "Numerical investigation of three-dimensionally evolving jets subject to axisymmetric and azimuthal perturbations," J. Fluid Mech. **230**, 271 (1991).
[42] P. A. Monkewitz and E. Pfizenmaier, "Mixing by side jets in strongly forced and self-excited round jets," Phys. Fluids **3**, 1356 (1991).
[43] M. Abid and M. E. Brachet, "Numerical characterization of the dynamics of vortex filaments in round jets," Phys. Fluids **5**, 2582 (1993).
[44] P. Brancher, J. M. Chomaz, and P. Huerre, "Direct numerical simulations of round jets: Vortex induction and side jets," Phys. Fluids **6**, 1768 (1994).
[45] I. Danaila, J. Dusek, and F. Anselmet, "Coherent structures in a round, spatially evolving, unforced, homogenous jet at low Reynolds numbers," Phys. Fluids **9**, 3323 (1997).
[46] S. Raghu, B. Lehmann, and P. A. Monkewitz, "On the mechanism of side-jet generation in periodically excited axisymmetric jets," Adv. Turbul. 3 (Springer-Verlag, Stockholm, 1990), 221.
[47] S. E. Widnall, D. B. Bliss, and C. Y. Tsai, "The instability of short waves on a vortex ring," J. Fluid Mech. **66**, 35 (1974).
[48] C. Y. Tsai and S. E. Widnall, "The stability of short waves on a straight vortex filament in a weak externally imposed strain field," J. Fluid Mech. **73**, 721 (1976).
[49] A. Dazin, P. Dupont, and M. Stansilas, "Experimental characterization of the instability of the vortex ring, part I," Exp. Fluids **40**, 383 (2006).
[50] T. Hayase, J. A. C. Humphrey, and R. Greif, "A consistently formulated QUICK scheme for fast and stable convergence using finite-volume iterative calculation procedure," J. Comput. Phys. **98**, 108 (1992).
[51] S. V. Patankar, *Numerical Heat Transfer and Fluid Flow* (Taylor and Francis, 1980).
[52] M. Sussman, E. Fatemi, P. Smereka, and S. Osher, "An improved level set method for incompressible two-phase flows," Comput. Fluids **27**, 663 (1998).
[53] S. Osher and R. P. Fedkiw, "Level set methods: an overview and some recent results," J. Comput. Phys. **169**, 463 (2001).
[54] S. Dabiri, W. A. Sirignano, and D. D. Joseph, "Cavitation in an orifice flow," Phys. Fluids **19**, 072112 (2007).
[55] S. Dabiri, "Effects of cavitation on high pressure atomization," Ph.D. thesis (University of California, Irvine, 2009).
[56] S. Dabiri, W. A. Sirignano, and D. D. Joseph, "Two-dimensional and axisymmetric viscous flow in apertures," J. Fluid Mech. **605**, 1 (2008).
[57] D. Jarrahbashi, "Transient high-pressure fuel injection," Ph.D. thesis (University of California, Irvine, 2014).
[58] A. Mansour and N. Chigier, "Disintegration of liquid sheets," Phys. Fluids A **2**, 706 (1990).
[59] W. A. Sirignano and C. Mehring, "Review of theory of distortion and disintegration of liquid stream," Prog. Energy Combust. Sci. **26**, 609 (2000).
[60] G. Broze and F. Hussain, "Transition to chaos in a forced jet: intermittency, tangent bifurcations and hystresis," J. Fluid Mech. **311**, 37 (1996).
[61] G. S. Jiang and D. Peng, "Weighted ENO schemes for Hamilton-Jacobi equations," SIAM J. Sci. Comput. **21**, 2126 (1997).
[62] K. Karimi, "Characterisation of multiple-injection Diesel sprays at elevated pressures and temperatures," Ph.D. thesis (University of Brighton, 2007).